Supplemental information

Defect engineering over anisotropic

brookite toward substrate-specific

photo-oxidation of alcohols

S. M. Hossein Hejazi, Mahdi Shahrezaei, Piotr Błoński, Mattia Allieta, Polina M. Sheverdyaeva, Paolo Moras, Zdeněk Badura, Sergii Kalytchuk, Elmira Mohammadi, Radek Zbořil, Štěpán Kment, Michal Otyepka, Alberto Naldoni, and Paolo Fornasiero

Supplemental experimental procedures
Preparation of TiO₂ photocatalysts
Titanium (IV) bis (ammonium lactate) dihydroxide $Ti(NH_4C_3H_4O_3)_2(OH)_2$ aqueous solution (50 wt.%, Sigma–Aldrich) (TALH) and urea (ACS reagent, Sigma–Aldrich), were used as precursors for the synthesis of TiO_2 nanocrystals using a hydrothermal method, according to the procedure previously reported with some modifications[1–4]. A solution containing 45 mL of urea in deionized (DI) water and 5 mL of TALH was stirred until a clear solution was obtained. The solution was afterwards transferred to a 125 mL Teflon lined autoclave and placed in an oil bath at 180°C and stirred at this temperature with 800 rpm for 20 days. The autoclave was then cooled down in air and the precipitate was centrifuged and dispersed by sonication in DI water for several times until the pH of supernatant water became ~7. Finally, the precipitate was dried at 80°C for 12 h. To prepare pure brookite and pure anatase samples, 0.15M and 11.5M urea solution in DI water were used, respectively. Commercial TiO_2 brookite was purchased from Sigma-Aldrich (99.99 wt. % purity). To prepare the reduced powders, 20 mg of TiO_2 nanopowders were placed in a crucible within a quartz chamber in a tubular furnace (10 °C min⁻¹ heating/cooling ramp in N_2 flow rate 10 mL min⁻¹, 1 h dwell in H_2 flow rate 10 mL min⁻¹ at predefined temperature. Before starting the heat treatment, the tube furnace was cleaned up increasing the temperature up to 1000°C in air. 1 wt.% platinum nanoparticles were loaded on TiO_2 by a photodeposition method. Briefly, 50 mg of TiO_2 powder was suspended in 25 mL of methanol (ACS reagent, Sigma–Aldrich) and bubbled with Ar for 30 min. Then, a solution of $H_2PtCl_6\ 6H_2O$ (ACS reagent, Sigma–Aldrich) was added and stirred for 20 min in the dark to favor Pt adsorption on the TiO_2 surface. Then the solution was illuminated for 1h using a solar simulator equipped with a 150 W Xe arc lamp and an AM 1.5G filter and calibrated to deliver a power of 100 mW cm⁻² (1 Sun).

Characterization
The morphological analyses of the samples were performed by transmission electron microscopy (TEM) JEM-2100 (JEOL, Tokyo, Japan) at 200 kV of accelerating voltage. For TEM measurements, the samples were dispersed in ethanol by sonication for 5 minutes and then the suspensions were dropped on the copper grid with holey carbon film and dried upon air exposure. The average particle size of brookite nanorods were assessed by analyzing TEM micrographs and by considering at least 100 nanorods. The high-resolution transmission electron microscopy (HRTEM) analysis were performed using a HRTEM Titan G2 (FEI) with image corrector on accelerating voltage 300 kV. Images were taken with BM UltraScan CCD camera (Gatan).

X-ray diffraction (XRD) patterns were recorded at room temperature with an Empyrean (PANalytical, Almelo, The Netherlands) diffractometer in the Bragg-Brentano geometry and using Co-$K_α$ radiation (40 kV, 30 mA, $λ$ = 0.1789 nm). The diffractometer was equipped with a PIXcel3D detector and programmable divergence and diffracted beam anti-scatter slits. The same amount of powders was placed on a zero-background Si slide. The measurement range was 2θ = 10° - 100°, with a step size of 0.0167° and acquisition time of 4 s per step. Standards SRM640 (Si) and SRM660 (LaB_6) were used to evaluate the line position and the instrumental line broadening, respectively. The identification of crystalline phases was performed using the High Score Plus software that includes the PDF-4+ and ICSD databases. Rietveld analysis was performed through the GSAS program[5]. We use the brookite orthorhombic model of Pbca space group with Ti and two O, namely O1, O2, in 8c position (x,y,z)[6]. During the refinement, the background was subtracted using shifted Chebyshev polynomials and the diffraction peak profiles were fitted with a modified pseudo-Voigt function. In the last calculation cycles all the parameters were refined: cell parameters, atomic positional degrees of freedom, isotropic thermal parameters, anisotropic microstrain broadening parameters, background, diffractometer zero point. To evaluate annealing T evolution ionic charge of Ti from the experimental dTi-O1, dTi-O2 of brookite, we calculated the Bond Valence Sum (BVS) by using the tabulated parameters[7]. Crystallite size of synthesized brookite samples was estimated through the Williamson-Hall (WH) method[8] employing at least 15 reflections for each calculation. Single peak fitting to extract peak positions and profile parameters was performed through the WinPLOTR Software[9]. The crystallite size of as received and reduced commercial brookite and anatase was calculated from XRD patterns according to the Scherrer equation as follows:

$$D = \frac{K \times λ}{β \times cosθ}$$

where, D is the mean size of crystallite, K is the dimensionless shape factor, λ is the x-ray wavelength, β is the full width half maximum intensity (FWHM), and θ is the Bragg angle and considering K=0.9, λ=1.79 Å (Co).

Raman spectra were collected using a DXR Raman spectrometer (Thermo Scientific, Massachusetts, USA). The excitation laser operated at the wavelength of 455 nm. The samples were deposited on a silicon wafer and the laser was focused on its surface and tuned to maximize the signal. The laser power on the sample was set to 0.1 mW cm^{-2} and exposure time was 3 s. The reported Raman spectra were averaged over 512 experimental microscans.

The surface area and pore size analyses were performed by means of N_2 adsorption/desorption measurements at 77 K on a volumetric gas adsorption analyzer 3 Flex (Micromeritics, Georgia, USA) up to 0.965 P/P$_0$. Prior the analysis, the sample was degassed under high vacuum (10^{-4} Pa) at 130°C for 12 hours, while high purity (99.999 %) N_2 and He gases were used for the measurements. The Brunauer–Emmett–Teller area (BET) was determined with respect to Rouquerol criteria[10] for N_2 isotherm.

The ultraviolet-visible diffuse reflectance spectra (UV-Vis DRS) of the fabricated samples were obtained by Specord 250 plus (Analytik Jena, Jena, Germany) spectrophotometer. An integrating sphere was used to collect the spectrum and a Spectralon reference sample was used to measure the background.

X-ray photoelectron spectroscopy (XPS) was carried out with a PHI 5000 VersaProbe II (Physical Electronics, Chanhassen, USA) spectrometer using an Al K$_α$ source (15 kV, 50 W). The obtained data were evaluated with the MultiPak software package (Ulvac-PHI Inc., Chigasaki, Japan). High-resolution spectra of C *1s* peaks were acquired by setting the pass energy to 23.500 eV and step size to 0.200 eV. The binding energy values were corrected considering the C *1s* peak at 284.8 eV as a reference. The spectral analysis included Shirley background subtraction and peak deconvolution using Gaussian functions.

Photoluminescence spectroscopy (PL) was performed on an FLS980 fluorescence spectrometer (Edinburgh Instruments, Livingston, United Kingdom) equipped with a R928P photomultiplier (Hamamatsu, Japan), with a 450 W xenon arc lamp as the excitation source for steady-state spectra and an EPL-375 picosecond pulsed diode laser ($λ_{em}$= 372 nm with a pulse width of 66.5 ps, a repetition rate of 10 MHz and an average power of 75 µW, Edinburgh Instruments) in conjunction with a time-correlated single-photon counting system for time-resolved photoluminescence measurements. Spectral correction curves were provided by Edinburgh Instruments. The emission of TRPL spectra were detected at 450 nm. PL decay curves were fitted using a multi-exponential function:

$$I(t) = \sum_{i=1}^{n} B_i \exp\left(-\frac{t}{\tau_i}\right), \sum_{i=1}^{n} B_i = 1,$$

Where, the fit parameter τ_i represents the decay time constant, B_i represents the normalized amplitude of each component, n is the number of decay times.

The amplitude weighted average decay lifetime τ_{ave} of the entire PL decay process reads as:

$$\tau_{ave} = \frac{\sum B_i \tau_i^2}{\sum B_i \tau_i}$$

A nitrogen bath cryostat holder Optistat/DNV (Oxford instruments, Abingdon, United Kingdom) was used to control the temperature of sample during measurements. Since the PL emission of TiO_2 is weak at room temperature and due to highly scattering nature of a typical nano-TiO_2 sample, the stray excitation light could be wrongly assigned as PL signal[11]. To avoid this, the PL spectra were measured at 80 K. Using low temperature condition results in slower non-radiative decay and brighter PL[11], which decreases the effect of stray light scattered by the sample. The powders in solid were pressed between two flat quartz slides and put into the chamber. N_2 and methanol were used to investigate the PL behavior of the TiO_2 samples in contact with different environments. The methanol was degassed with argon bubbling for 10 minutes before wetting the sample.

An in-depth analysis of the electronic structure of the samples was carried out at the VUV-Photoemission synchrotron beamline (Elettra, Trieste) at room temperature with a Scienta R-4000 electron spectrometer. The O *1s* and Ti *2p* core levels were measured with photon energy 650 eV with an instrumental energy resolution of 0.2 eV. The valence band was probed in near-resonant conditions to the Ti L$_{2,3}$ edge, in order to enhance the signal of Ti-related states. A photon energy of 468 eV (energy resolution 0.14 eV) was used to avoid the appearance of spurious Ti *2p* signal in the region of interest (from 4 eV binding energy up to the Fermi level), due to high harmonics contribution from the beamline.

Electron paramagnetic resonance (EPR) spectra were recorded using a continuous wave X-band JEOL JES-X-320 spectrometer operating at ~9.1 GHz. The EPR spectrometer is equipped with a variable temperature control ES 13060DVT5 apparatus. The cavity Q quality factor was kept above 6000 in all measurements. Highly pure quartz tubes were used (Suprasil, Wilmad, ≤ 0.5 OD) and accuracy on *g*-values was obtained against a Mn^{2+}/MgO standard (JEOL standard). For all experiments the same acquisition conditions were kept. The microwave power was set to 1.5 mW, therefore, no power saturation effects was

occurring in the EPR traces. The modulation width of 0.7 mT and modulation frequency 100 Hz were used. Experimental temperature was set to 77 K. All spectra were recorded with 30 ms time constant and 2 min sweep time with 3 accumulations, to improve signal to noise ratio. A HeCd (200 mW) laser with 325 nm wavelength was employed as the UV light source during EPR experiments. EPR envelopes were simulated in Matlab software where the spin-Hamiltonian EasySpin simulation package[12] was implemented. During the measuring the samples in contact with DI water and methanol solution at 80K, the head space of EPR tube was purged by nitrogen to avoid any parasitic oxygen signals coming from the air. The EPR cavity was kept in constant flow of nitrogen to eliminate the formation of ice. The samples were measured in suspension form. For each experiment 10 mg of the powder and 100 µL of DI water/methanol mixture were used. In all experiments, to make spectra more comparable, the position of the EPR tube inside the cavity was kept the same.

^{1}H-NMR (proton nuclear magnetic resonance) spectra were obtained on a JEOL 400 MHz spectrometer in CD_3OD, using dimethyl sulfoxide (DMSO) as the internal standard. All the measurements were collected at ambient temperature with a spectral width of 20 ppm, a pulse width of 5.7 µs (90°), a relaxation delay of 60 s, and 8 scans. Chemical shifts (δ) are expressed in ppm.

C, H and N elemental analyses was performed on a Flash EA 1112 instrument (Thermo Finnigan, North Carolina, USA).

Pt loading on TiO_2 was determined by ICP-MS (Agilent 7700x, Agilent, USA) at isotope 105 using He mode and an external calibration. Calibration solutions were prepared from a certified reference material with Pt concentration 100,0 +/- 0,2 mg/L (Analytika Ltd., Czech Republic). A mixture of nitric acid (ACS reagent, 70%, Sigma–Aldrich) and hydrochloric acid (ACS reagent, 37%, Sigma–Aldrich) in a molar ratio of 1:3, was used to digest the Pt. The Pt loading in pristine and reduced brookite nanorods was 0.98 and 0.90%, respectively.

The hydrodynamic diameter of the brookite B700 was measured by Dynamic Light Scattering (DLS) at 23°C, using a Malvern Nano-ZS instrument (Malvern Ltd., Leamington Spa, UK). The light source was a laser 633 nm with power of 4 mW. The measurement was performed at the beginning (time = 0 h) and after specific times of reaction. The sample was taken from 10 mL of DI water and methanol (1:1 vol) solution with 2 mg of dispersed B700-Pt. At time = 0h the solution was ultrasonically dispersed for 10 min.

Photocatalytic experiments

Photocatalytic activity was measured in a quartz reactor with 10 mL solution of DI water and methanol (volume ratio 1:1). The same conditions and volume ratio were applied for the photocatalytic reactions with ethanol (99.8%, BC Chemservic), isopropanol (ACS reagent, 99.8%, Sigma–Aldrich), formaldehyde (36-38%, Penta), and formic acid (99%, Penta). After sealing the reactor with a rubber septum, the photocatalysts were sonicated for 10 min to create a homogeneous suspension. Afterwards, the suspension was bubbled with argon for 30 min to remove the unwanted gasses and dissolved oxygen. The samples were irradiated using a solar simulator equipped with a 150 W Xe arc lamp and an AM 1.5G filter and calibrated to deliver a power of 100 mW cm^{-2} (1 Sun). A calibrated reference solar cell (Newport, California, USA) was used before and after reaction to check the power of irradiation. Each sample was irradiated for 24 h under continuous stirring before measuring the amount of evolved hydrogen. The test was repeated three times and the average amount of measured hydrogen was reported. The photocatalytic hydrogen was detected with a gas chromatograph GCMS-QP2010 SE (Shimadzu, Kyoto, Japan) and a TCD (Thermal conductivity detector), using Ar as carrier gas. The temperature of the reaction suspension was measured with a thermocouple and was 23°C both before and after 24 h of irradiation under 1 Sun illumination.

To identify the wavelength dependence of AQY, the reactor was illuminated with the wavelengths 316 (1.6 mW cm^{-2}), 334 (1.2 mW cm^{-2}), 360 (2.8 mW cm^{-2}), 369 (8.7 mW cm^{-2}), 386 (5 mW cm^{-2}) and 402 nm (17.7 mW cm^{-2}) using a tunable diode light source of Zahner CIMPS PP201 system. The illuminated surface area was 0.94 cm^2 and the power of each wavelength was measured using an external digital power meter Thorlabs PM100D. The sample was illuminated for 1h and the reacting medium was a 1:1 vol/vol% water:methanol mixture. The apparent quantum yield (AQY) was calculated according to the following equation:

$$AQY = \frac{Number\ of\ reacted\ electrons}{Number\ of\ incident\ photons} \times 100 = \frac{2 \times Number\ of\ evolved\ H_2\ molecules}{Number\ of\ incident\ photons}$$

The qNMR (quantitative nuclear magnetic resonance) analysis was used to investigate the rate of methanol consumption during the photocatalytic hydrogen evolution. For this purpose, a 10 mL mixture of DI water:

CD$_3$OD (volume ratio 1:1) was prepared. To have a detectable signal, 50 μL of non-deuterated methanol (i.e. CH$_3$OH) was added to the above mixture. The photocatalytic experiment was performed following the same procedure explained above for hydrogen evolution measurements. At the specified times, 600 μL of solution was taken by a syringe and centrifuged at 15000 rpm for 30min to separate the catalyst. Then the clear and transparent solution was transferred to a quartz NMR tube and 0.2 μL DMSO was added as internal standard. The NMR spectra of the samples were recorded and the peak area of methanol at 3.32 ppm was compared to the peak area of internal standard to study the rate of photocatalytic methanol consumption over time. The photocatalytic activity of pristine and reduced samples functionalized with Pt nanoparticles (brookite nanorods, commercial brookite, and anatase nanocrystals) were optimized by varying the amount of catalyst. The optimized photocatalyst amount needed to reach the maximum photocatalytic activity was 2 mg for brookite nanorods, and 4 g for both commercial brookite and anatase nanocrystals.

DFT calculations

Calculations were carried out by using the DFT-based Vienna Ab Initio Simulation Package (VASP)[13,14]. The projector-augmented-wave (PAW) formalism[15,16] was used to treat the electron–ionic core interactions. A plane-wave basis with a 400 eV energy cutoff was used. Test calculations were also performed with energy cutoff increased to 600 eV. Exchange and correlation effects were treated within a generalized-gradient approximation (GGA) by using Perdew-Burke-Ernzerhof (PBE) functional[17,18]. To counteract the problems of standard density functionals associated with the self-interaction error (SIE) we applied on-site Hubbard corrections[19] to both Ti-d and O-p states[20] with an effective U parameter of 6 eV. All computations were performed in spin unrestricted manner. Brillouin zone samplings were kept restricted to Gamma point only due to the supercell dimensions being sufficiently large. We modeled the (210) surface of brookite by a bulk-terminated slab of 12 Ti-layers in thickness and 14.38 Å × 15.41 Å of surface area and containing 432 atoms (see the structure shown in Figure S46)[21], and with a vacuum layer of length ~20 Å deployed along the off-planar direction to ward off spurious interactions with the periodic images. Except atoms in the middle part of the slab (area enclosed by green planes in the structure displayed in Figure S46), all other atoms were relaxed until all forces were reduced below 0.025 eV Å^{-1} and the change in total energy between successive iteration steps became smaller than 10^{-6} eV.

Several possible sites for oxygen vacancy formation were considered (and denoted by V1–V8 in the structure in Figure S46) and the system was re-optimized. For oxygen vacancy defects present in the bulk region of the slab, atoms in the immediate vicinity of the vacancy were allowed to relax too.

The effect of distortion of TiO$_6$ octahedra on the electronic structure of brookite was also considered. Two models were considered: (i) Several Ti-O axial distances were modified by up to ±0.1 Å and the change in densities of states with respect to an ideal (210) surface of brookite was monitored. (ii) Randomly chosen Ti-O distances were modified within ±0.1 Å and accompanied by a displacement of Ti atoms from its equilibrium positions.

Table S1. Digital photographs of investigated samples. Digital photographs of as synthesized brookite (B-AS), as-received commercial brookite (CB-AR), as-synthesized anatase (A-AS) and reduced samples at different temperatures. The numbers after abbreviations stand for reducing temperature in °C.

Sample		Sample		Sample	
B-AS		CB-AR		A-AS	
B500		CB400		A400	
B600		CB500		A500	
B700		CB600		A600	
B800		CB700		A700	
B900		CB800			
B1000					

Note S1. Related to Table S1. Upon reduction under hydrogen atmosphere at different temperatures, the color of synthesized brookite and anatase samples changed from white to gray and black, while the commercial brookite showed a relatively small color change (Table S1), suggesting its non-reducibility, as also confirmed by the other characterizations reported below.

Table S2. CHN elemental analysis. CHN analysis of the pristine and the most photoactive sample for brookite, commercial brookite and anatase.

Sample	C (wt. %)	H (wt. %)	N (wt. %)
B-AS	0.25 ± 0.08	0.27 ± 0.03	0.12 ± 0.03
B700	0.19 ± 0.02	0.07 ± 0.01	0.03 ± 0.01
CB-AR	1.22 ± 0.04	0.83 ± 0.02	0.07 ± 0.01
CB600	0.73 ± 0.05	0.08 ± 0.01	0.09 ± 0.03
A-AS	1.03 ± 0.06	1.43 ± 0.09	0.11 ± 0.02
A-500	0.39 ± 0.06	0.16 ± 0.05	0.06 ± 0.02

Note S2. Related to Table S2. To exclude the contribution of carbon, nitrogen, and hydrogen impurities to the photocatalytic activity, CHN analysis of TiO_2 samples were carried out before and after reduction under hydrogen atmosphere for the most active photocatalysts. As Table S2 shows, there is no significant difference between carbon, nitrogen, and hydrogen concentrations in the samples before and after the thermal treatment in hydrogen.
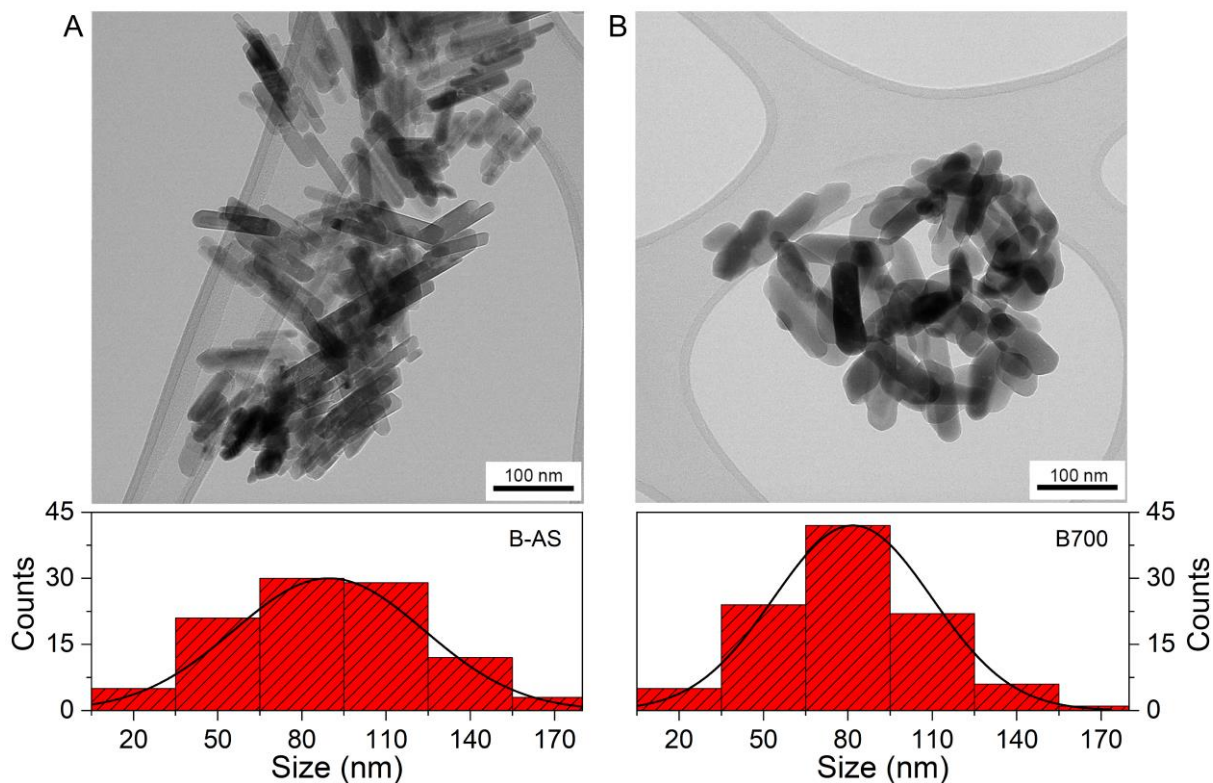
Figure S1. Morphology of TiO_2 photocatalysts, related to Figure 1. TEM images of (A) B-AS and (B) B700 with associated histograms of size distributions (bottom) based on 100 measurements of nanorods length.
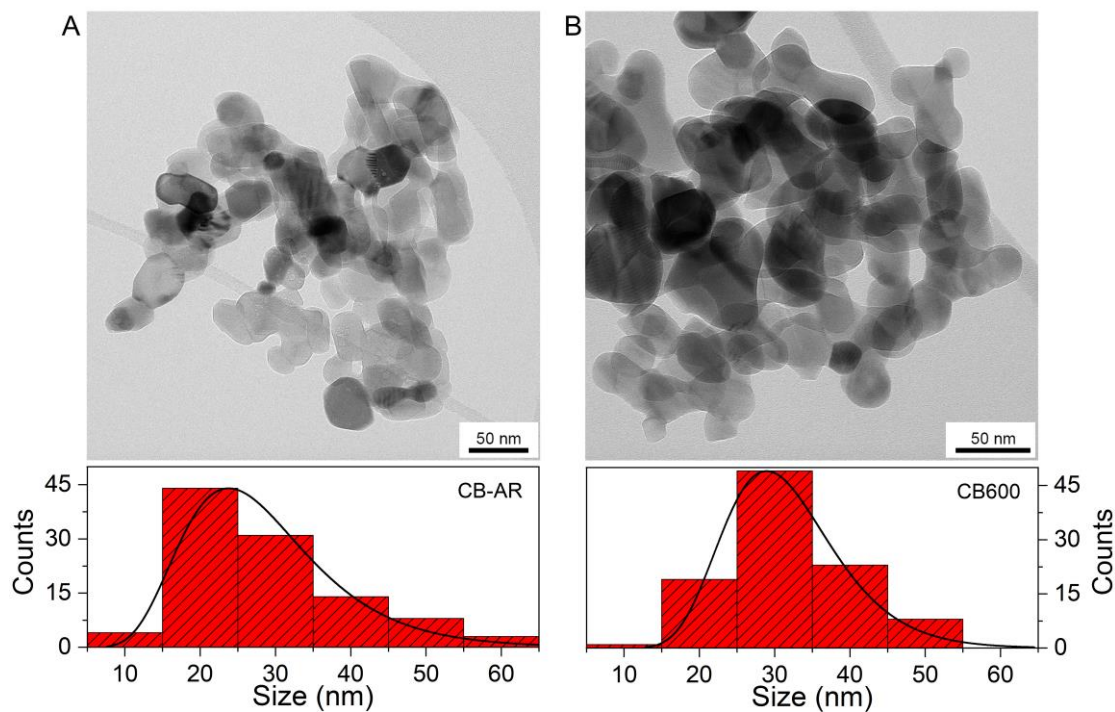
Figure S2. Morphology of TiO₂ photocatalysts, related to Figure 1. TEM images of (A) CB-AR and (B) CB600 with associated histograms of size distributions (bottom) based on 100 measurements of particle diameter.
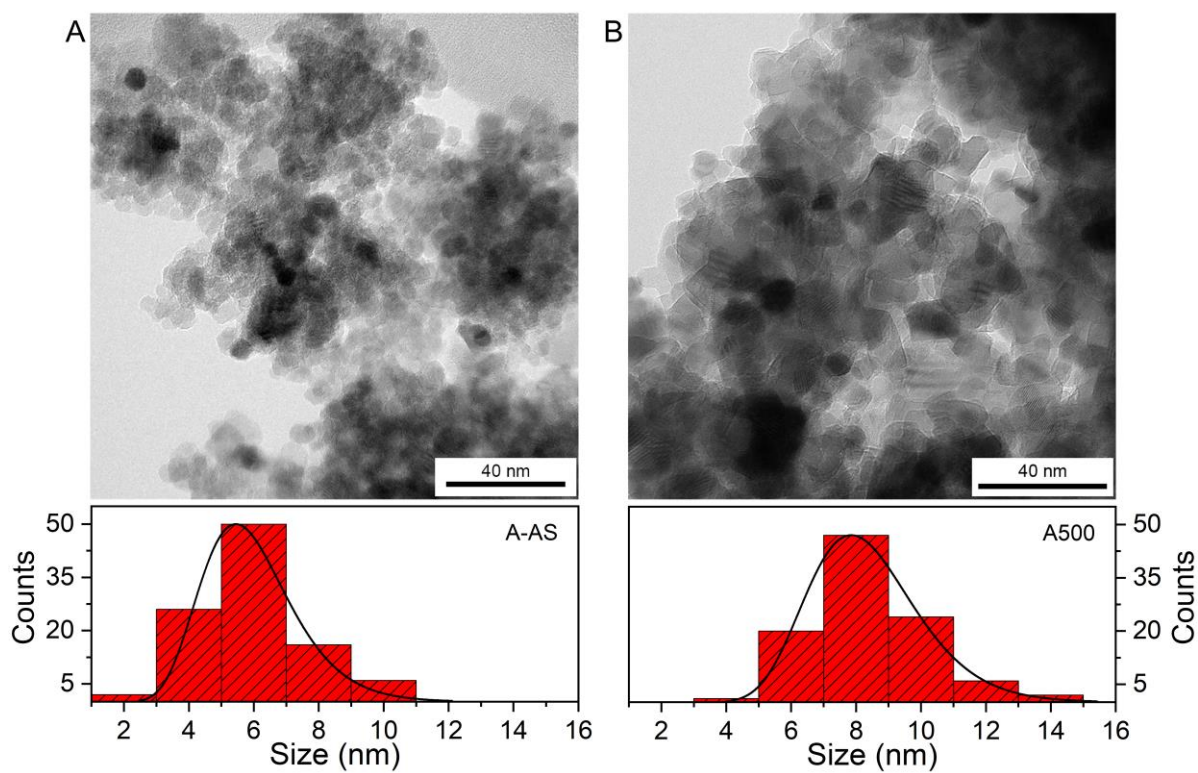

Figure S3. Morphology of TiO₂ photocatalysts, related to Figure 1. TEM images of (A) A-AS and (B) A500 with associated histograms of size distributions (bottom) based on 100 measurements of particle diameter.

Note S3. Related to Figures S1–S3. Figure S1A and Figure S1B show the TEM images of B-AS and B700, respectively. The as-synthesized brookite nanorods have an average length of 90 ± 35 nm that after reduction under hydrogen atmosphere at 700°C decreased to 82 ± 28 nm. However, the reduction in high temperature resulted in aggregation of particles due to sintering as well as losing their well-defined facets. Figure S2A and Figure S2B present the TEM images of CB-AR and CB600, respectively. The particle shape of commercial brookite is rounded (average diameter 29 ± 10 nm) in comparison with the synthesized brookite and showed almost no change in shape and a slightly increase in size after reduction (average diameter 32 ± 7 nm). The as synthesized anatase is spherical in shape with average diameter of 6 ± 1 nm (Figure S3) and its shape remained unchanged with slighty increase in diameter after reduction (average diameter 8 ± 2 nm).
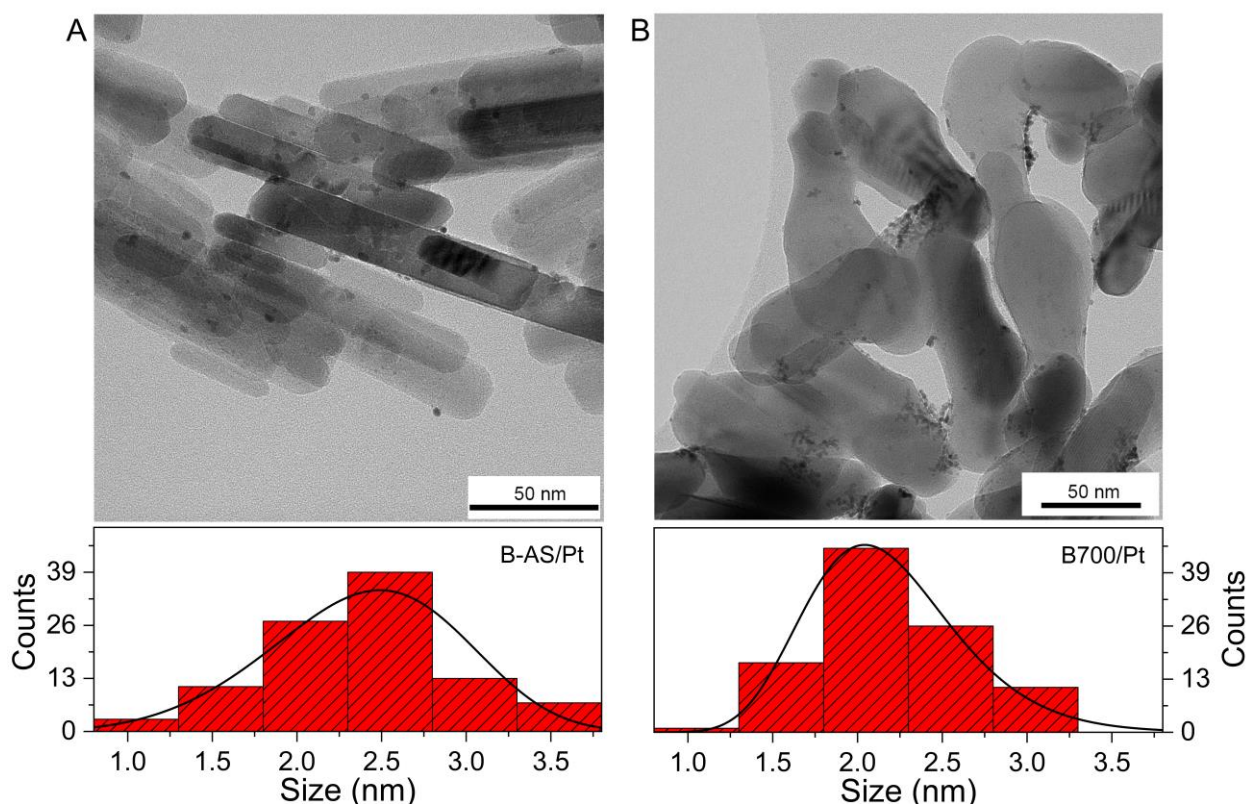
Figure S4. Morphology of TiO$_2$/Pt photocatalysts, related to Figure 1. TEM images of (A) platinized pristine brookite and (B) platinized reduced brookite at 700°C with associated histograms of size distributions of Pt particles (bottom) based on 100 measurements of particle diameter. The loaded reduced brookite present large Pt aggregates and therefore the size distribution refers to the isolated Pt nanoparticles found in the sample. The photodeposition of Pt results clearly in different results: pristine brookite present isolated homogeneously dispersed Pt nanoparticles, while reduced brookite show mainly large Pt aggregates and some isolated Pt nanoparticles.
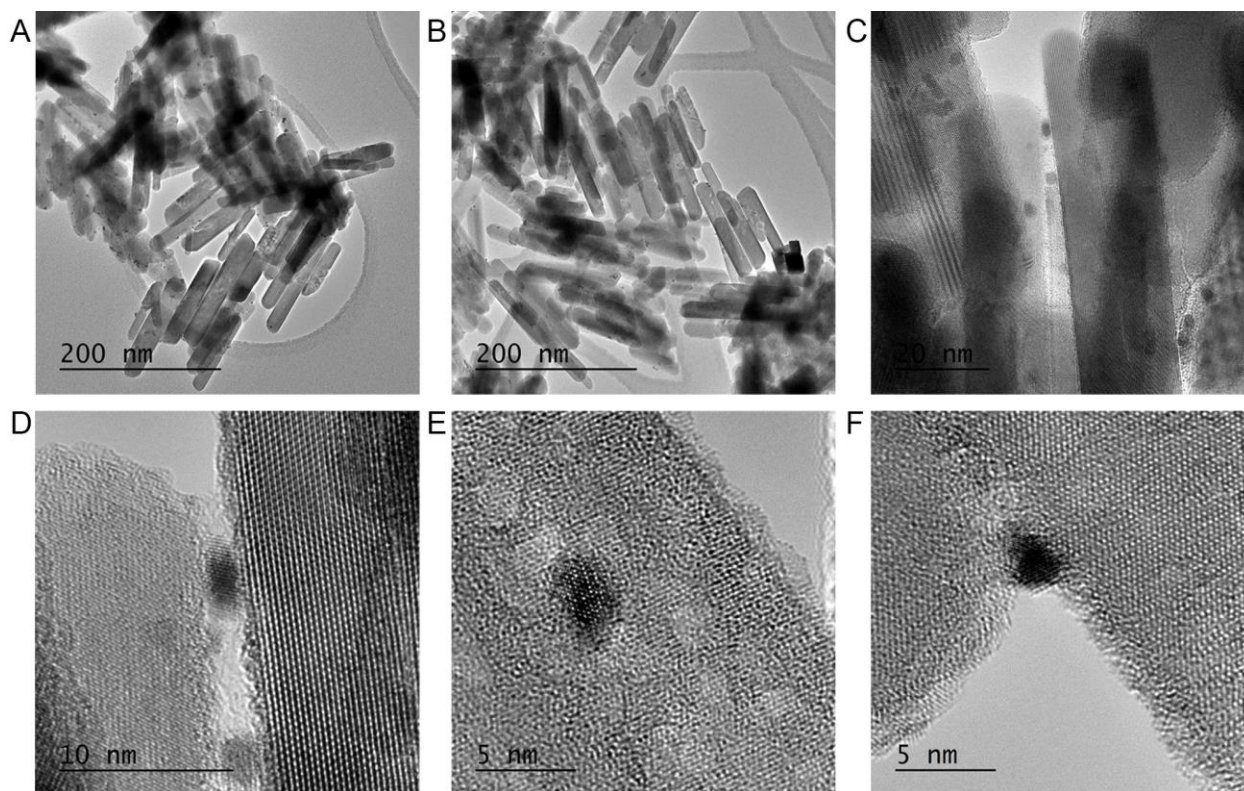
Figure S5. Morphology of TiO$_2$/Pt photocatalysts, related to Figure 1. (A,B) TEM and HR-TEM (C-F) micrographs of pristine brookite nanorods loaded with 1 wt% Pt showing their homogeneous distribution over the TiO$_2$ matrix. The darker dots are the Pt nanoparticles.
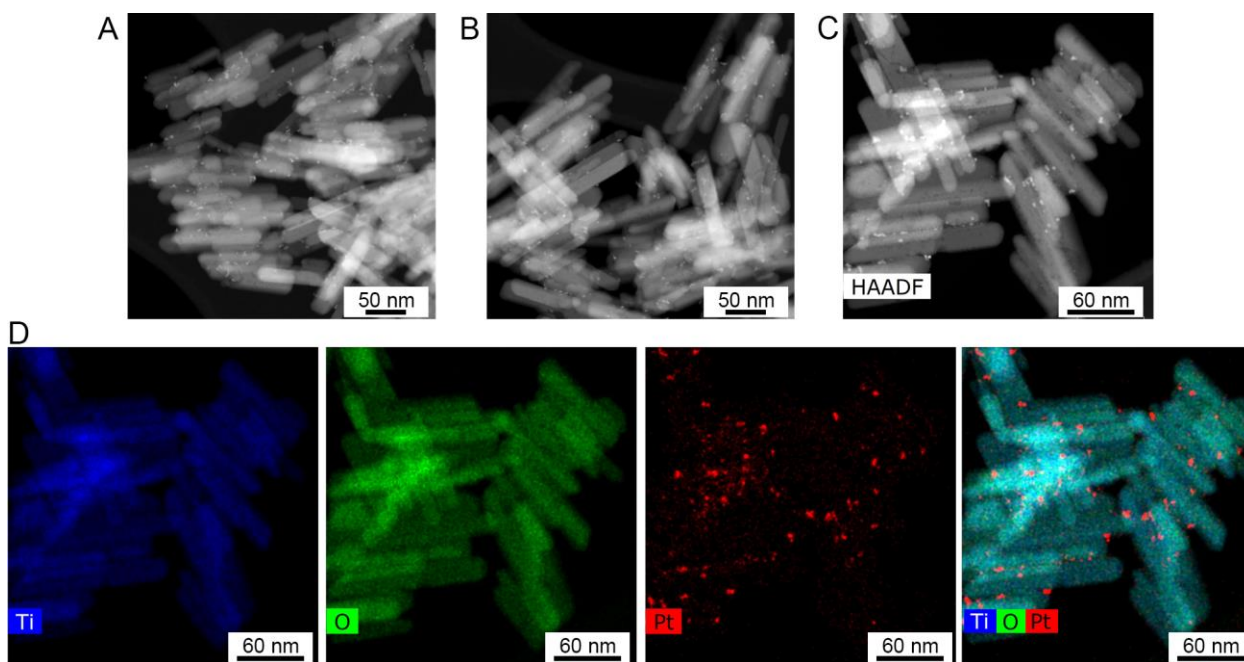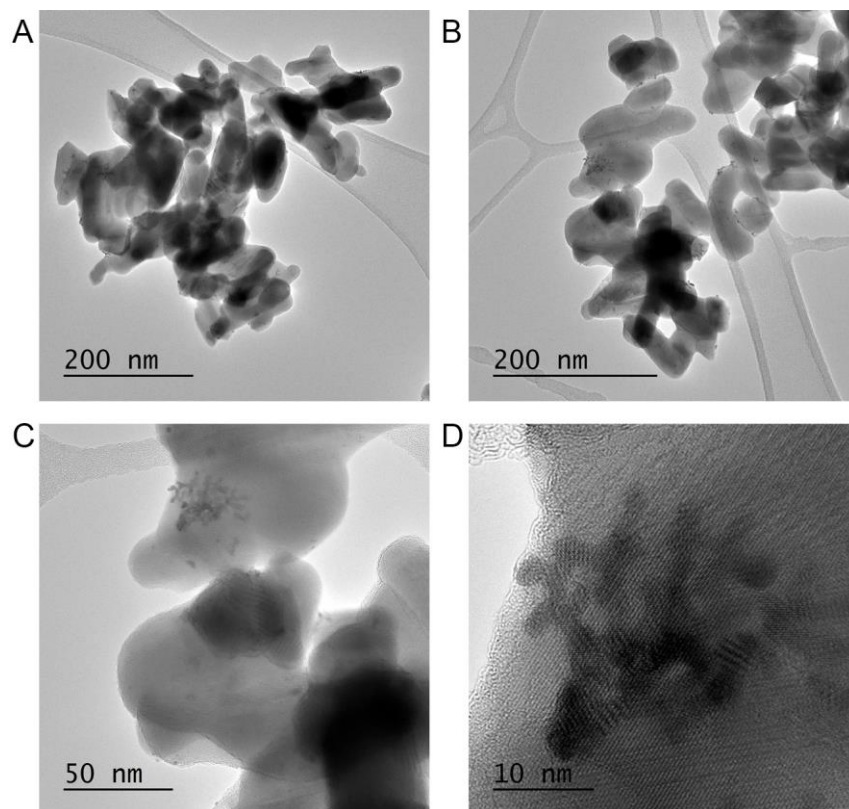

Figure S6. Morphology of TiO$_2$/Pt photocatalysts, related to Figure 1. (A-C) STEM-HAADF images and (D) elemental EDS mapping of (C) for pristine brookite nanorods loaded with 1 wt% Pt showing their homogeneous distribution over the TiO$_2$ matrix.

Figure S7. Morphology of TiO₂/Pt photocatalysts, related to Figure 1. (A-C) TEM and HR-TEM (D) of micrographs reduced brookite nanorods (at 700°C) loaded with 1 wt% Pt showing their aggregation over the TiO₂ matrix. The darker dots and nanostructured aggregates are made by Pt.
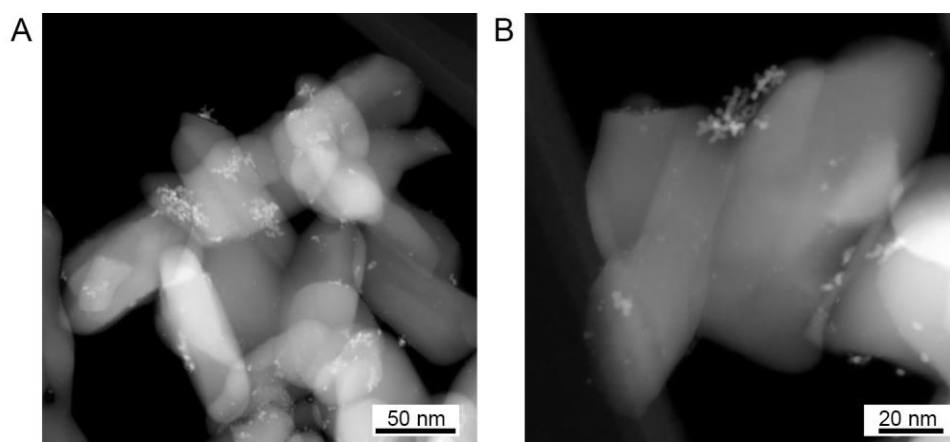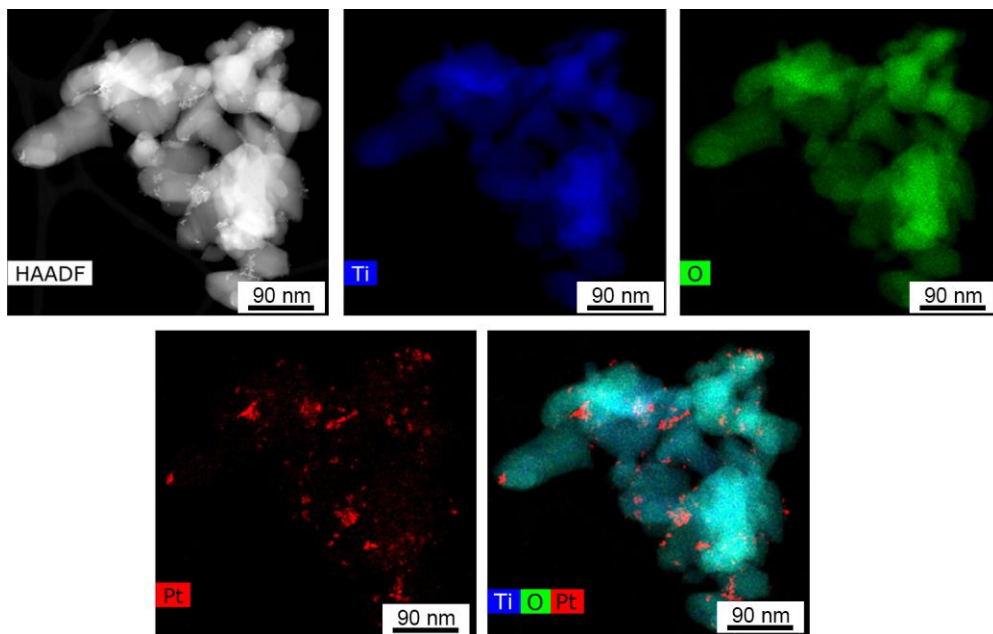

Figure S8. Morphology of TiO₂/Pt photocatalysts, related to Figure 1. (A-C) TEM and HR-TEM (D) of micrographs reduced brookite nanorods (at 700°C) loaded with 1 wt% Pt showing their aggregation over the TiO₂ matrix. The Pt nanocrystals are the brighter spots.

Figure S9. Morphology of TiO₂/Pt photocatalysts, related to Figure 1. STEM-HAADF and elemental mapping images of reduced brookite nanorods (at 700°C) loaded with 1 wt% Pt showing their aggregation over the TiO₂ matrix.
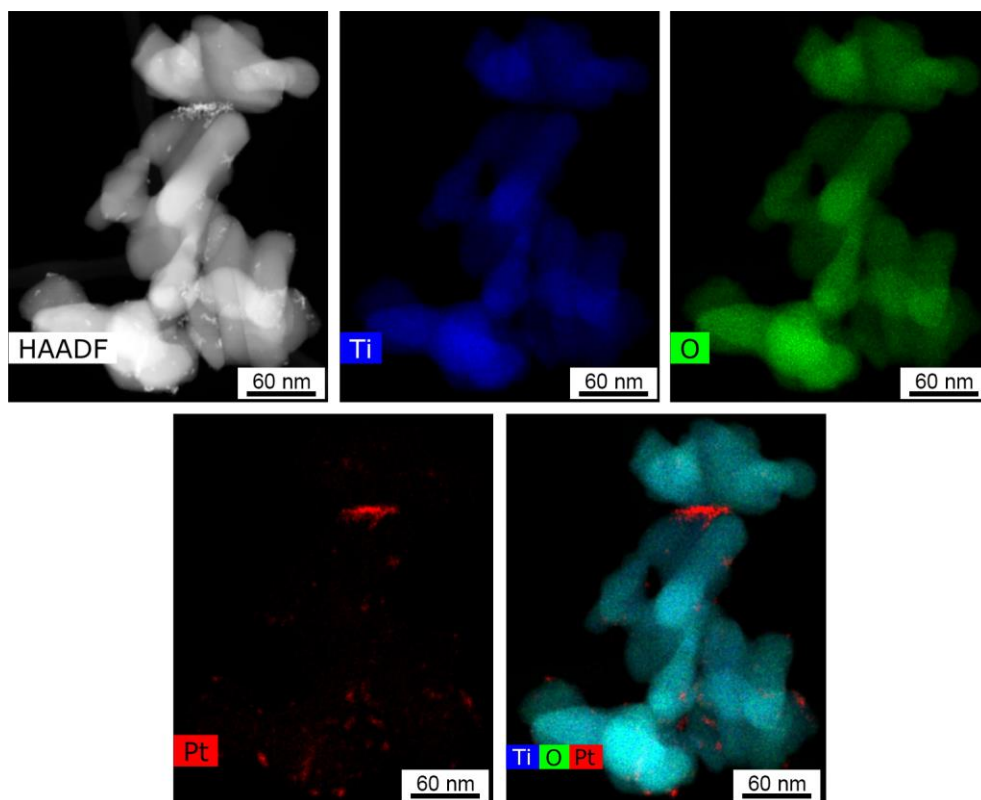

Figure S10. Morphology of TiO₂/Pt photocatalysts, related to Figure 1. STEM-HAADF and elemental mapping images of reduced brookite nanorods (at 700°C) loaded with 1 wt% Pt showing their aggregation over the TiO₂ matrix.
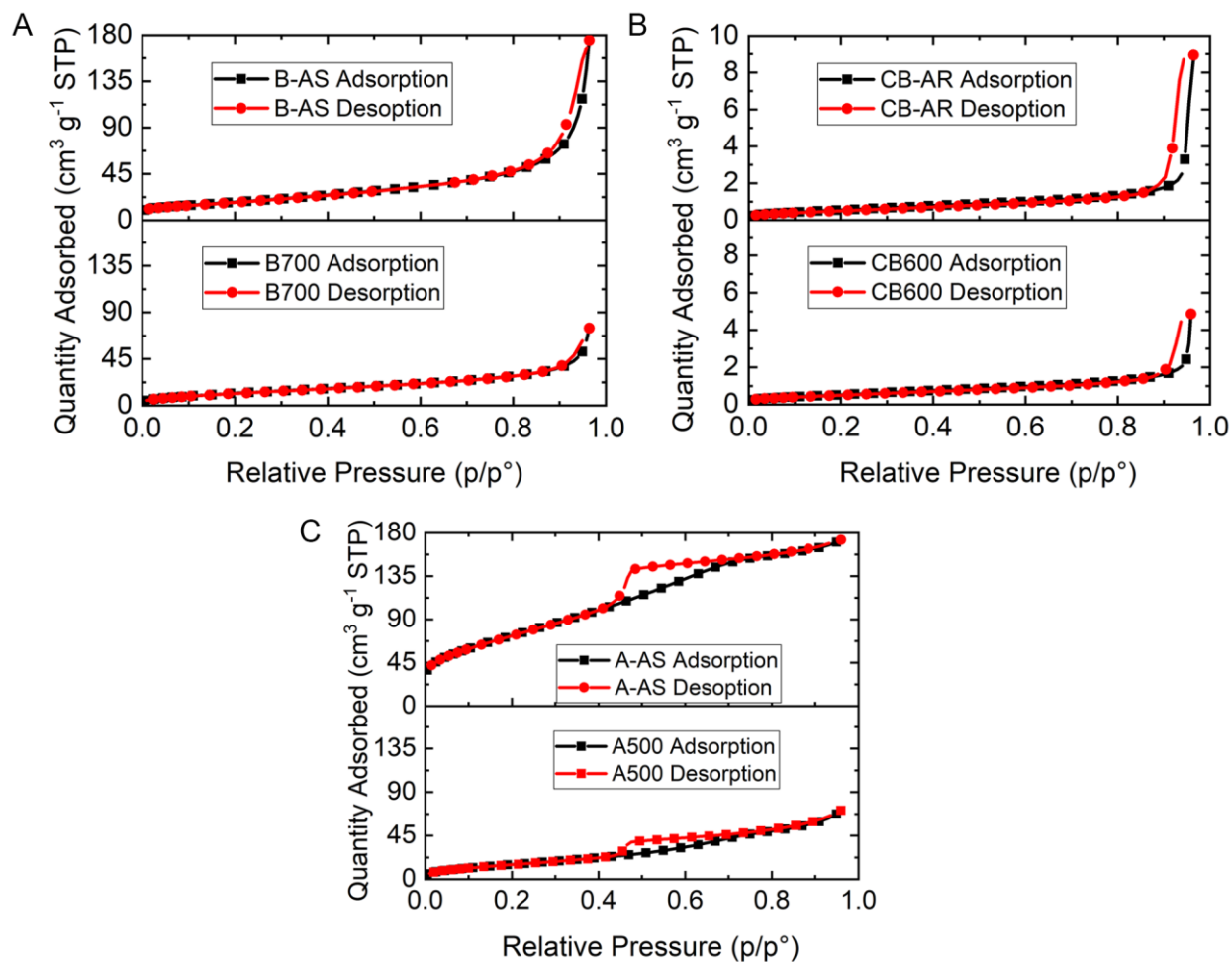
Figure S11. Specific surface area measurement, related to Figure 1. N_2 adsorption/desorption type IV isotherms (mesoporous solids) at 77K for (A) B-AS and B700, (B) CB-AR and CB600, and (C) A-AS and A500.

Table S3. Specific surface area, related to Figure 1. Brunauer−Emmett−Teller (BET) specific surface area for the pristine and the most photoactive sample of each studied phases of TiO_2.

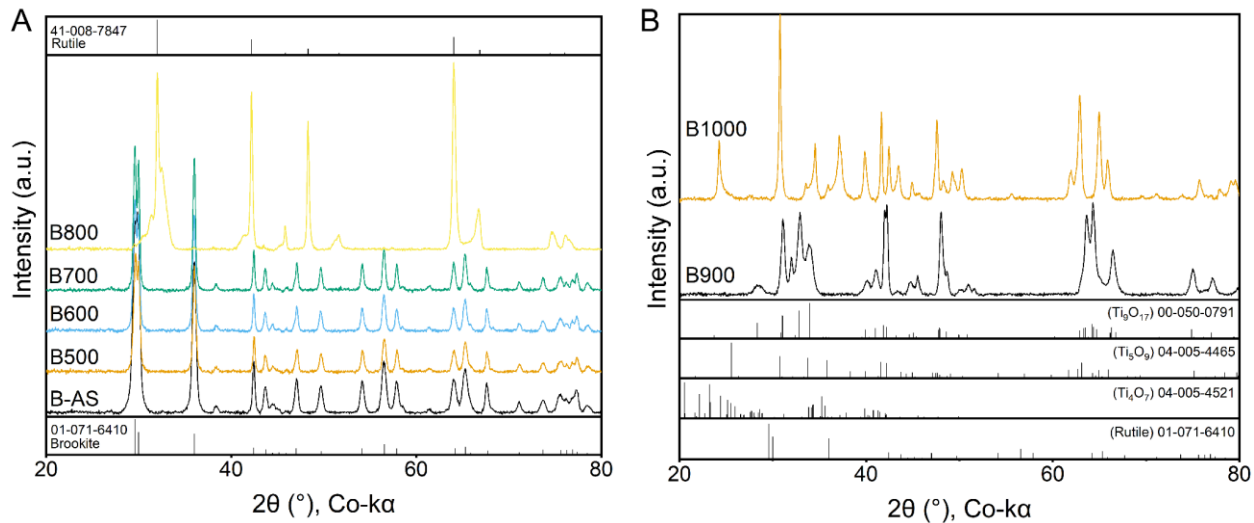| Sample	BET surface area (m^2 g^{-1})
B-AS	67
B700	47
CB-AR	50
CB600	48
A-AS	273
A-500	189

Figure S12. X-ray diffraction patterns. (A) XRD patterns of brookite samples and reference patterns for brookite (bottom) and rutile (top). (B) XRD patterns for reduced brookite at 900 and 1000 °C and reference patterns (bottom) for rutile and various magnéli phases (Ti_xO_{2x-1}).
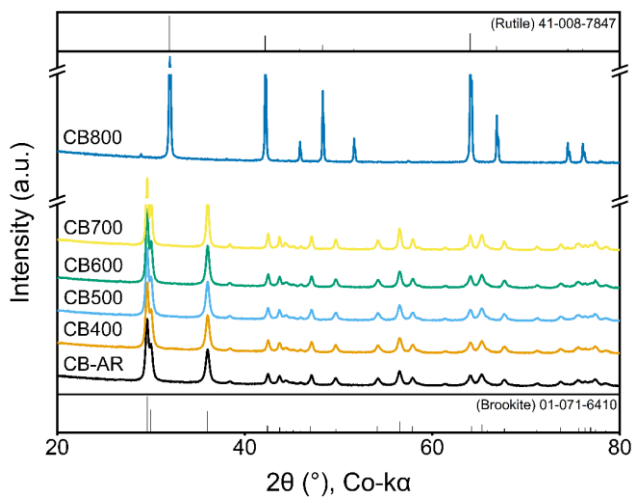

Figure S13. X-ray diffraction patterns. XRD patterns for commercial brookite samples and reference patterns for brookite (bottom) and rutile (top).
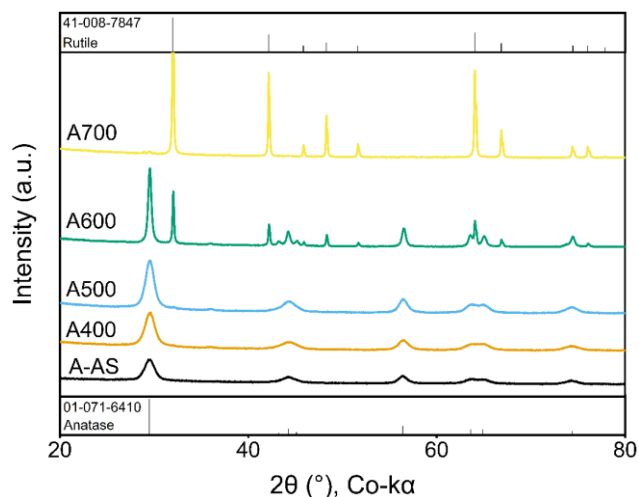
Figure S14. **X-ray diffraction patterns.** XRD patterns for anatase samples and reference patterns for anatase (bottom) and rutile (top).

Table S4. **Phase composition brookite nanorods, related to Figure S12.** Phase composition of brookite samples retrieved from Rietveld refinement of XRD patterns.

Sample	Brookite (wt.%)	Rutile (wt.%)	Ti_4O_7 (wt.%)	Ti_5O_9 (wt.%)	Ti_9O_{17} (wt.%)
B-AS	100	-	-	-	-
B500	100	-	-	-	-
B600	100	-	-	-	-
B700	100	-	-	-	-
B800	9	91	-	-	-
B900	-	9	-	-	91
B1000	-	-	94	6	-

Table S5. Phase composition commercial brookite, related to Figure S13. Rietveld quantitative phase analysis of commercial brookite samples and crystallite size calculated according to the Scherrer method.

Sample	Brookite (wt.%)	Anatase (wt.%)	Rutile (wt.%)	Crystallite size (nm)
CB-AR	100	-	-	27
CB400	100	-	-	27
CB500	100	-	-	28
CB600	100	-	-	31
CB700	100	-	-	41
CB800	-	-	100	69

Table S6. Phase composition anatase, related to Figure S14. Rietveld quantitative phase analysis of anatase samples and crystallite size calculated according to the Scherrer method.

Sample	Anatase (wt.%)	Rutile (wt.%)	Crystallite size (nm)
A-AS	100	-	8
A400	100	-	8
A500	100	-	13
A600	68	32	24
A700	-	100	28
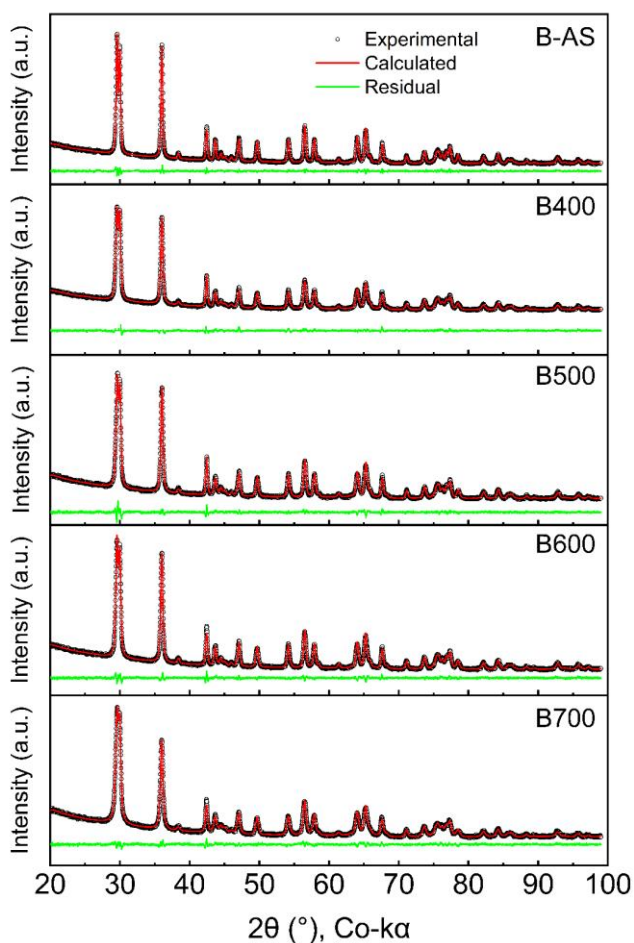
Figure S15. Rietveld refinements of brookite samples reduced at different temperatures, related to Figure S16−S19. Dots are experimental data; continuous lines are the calculated profiles; Rietveld agreement factors [R (F2)] between observed and calculated patterns ranged from 0.06 to 0.08.
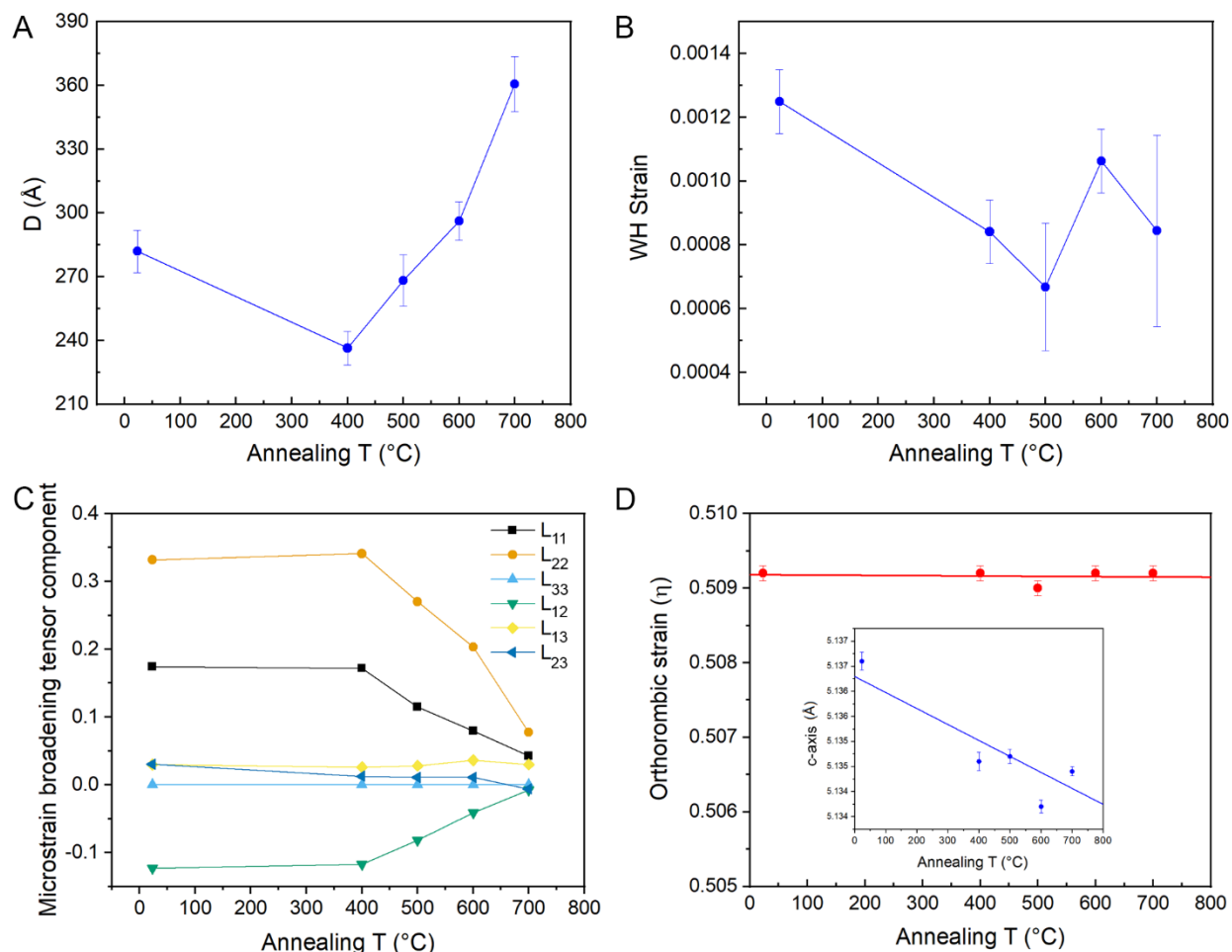
Figure S16. Structural parameters of brookite samples reduced at different temperatures, related to Figure S15. Parameters retrieved from Rietveld refinements of XRD patterns for as synthesized brookite and brookite reduced at different temperatures (i.e. annealing T in x axis). (A) Reducing temperature dependence of average particle size (D), and (B) crystal structure strain as obtained by Williamson- Hall (WH) method. (C) Annealing temperature evolution of components of empirical extension of anisotropic microstrain broadening tensor (L) refined by Rietveld refinements. Indexes are referring to the following expression: L = $L_{11}h^2 + L_{22}k^2 + L_{33}l^2 + 2L_{12}hk + 2L_{13}hl + 2L_{23}kl$. (D) Annealing temperature dependence of orthorhombic strain (see text) and c-axis (inset).
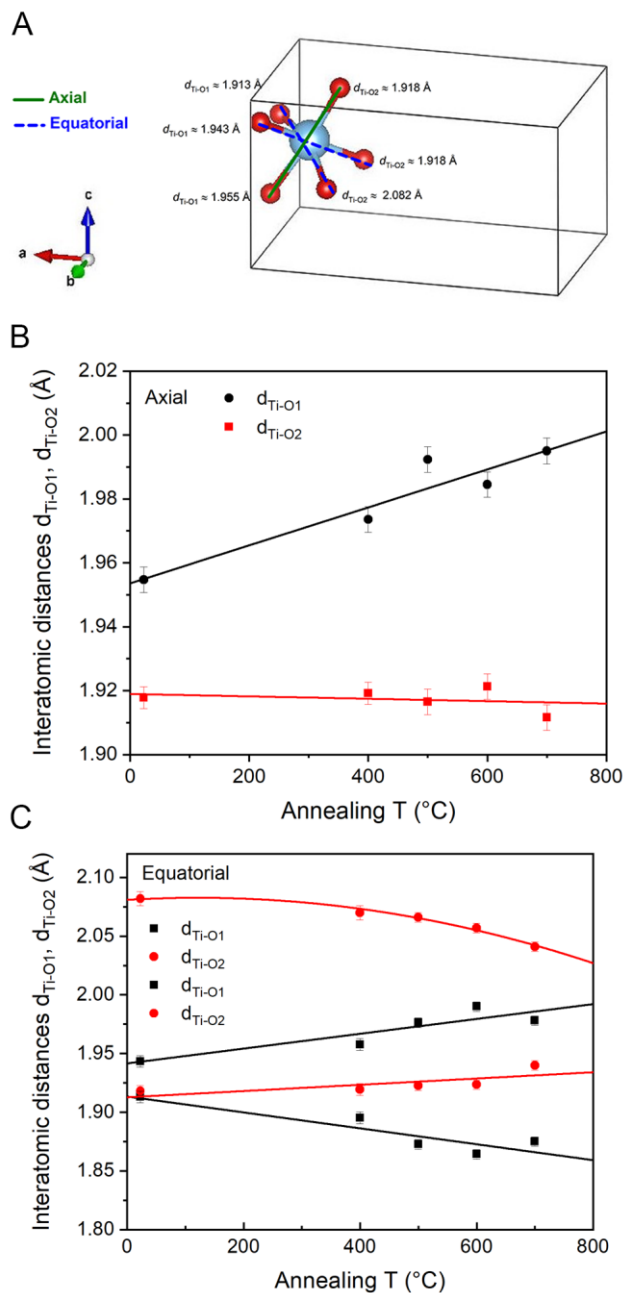
Figure S17. Structural parameters of brookite samples reduced at different temperatures, related to Figure S15. (A) Representation of octahedra (TiO_6) in TiO_2 brookite unit cell (Pbca) showing the arrangement of distorted TiO_6 resulting in two groups of distances, namely d_{Ti-O1} and d_{Ti-O2}, composed by two axial and four equatorial different interatomic distances. Values refer to structure refined at room temperature. (B) Evolution of axial and (C) equatorial interatomic distances retrieved from Rietveld refinements of XRD patterns for as synthesized brookite and brookite reduced at different temperatures (i.e. annealing T in x axis). Solid lines are guide to the eye.
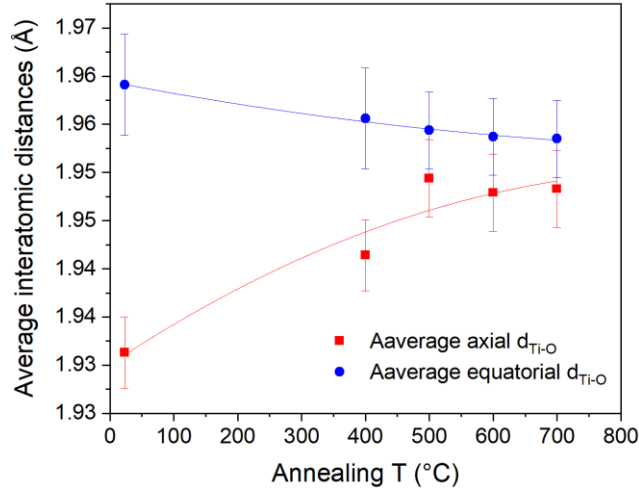
Figure S18. Structural parameters of brookite samples reduced at different temperatures, related to Figure S15. Annealing Temperature dependence of averaged axial and equatorial interatomic retrieved from Rietveld refinements of XRD patterns for as synthesized brookite and brookite reduced at different temperatures (i.e. annealing T in x axis).

Figure S19. Structural parameters of brookite samples reduced at different temperatures, related to Figure S15. (A) Annealing Temperature dependence of Ti Bond Valence Sum (BVS) and (B) correlation between Ti BVS and c-axis contraction retrieved from Rietveld refinements of XRD patterns for as synthesized brookite and brookite reduced at different temperatures (i.e. annealing T in x axis).
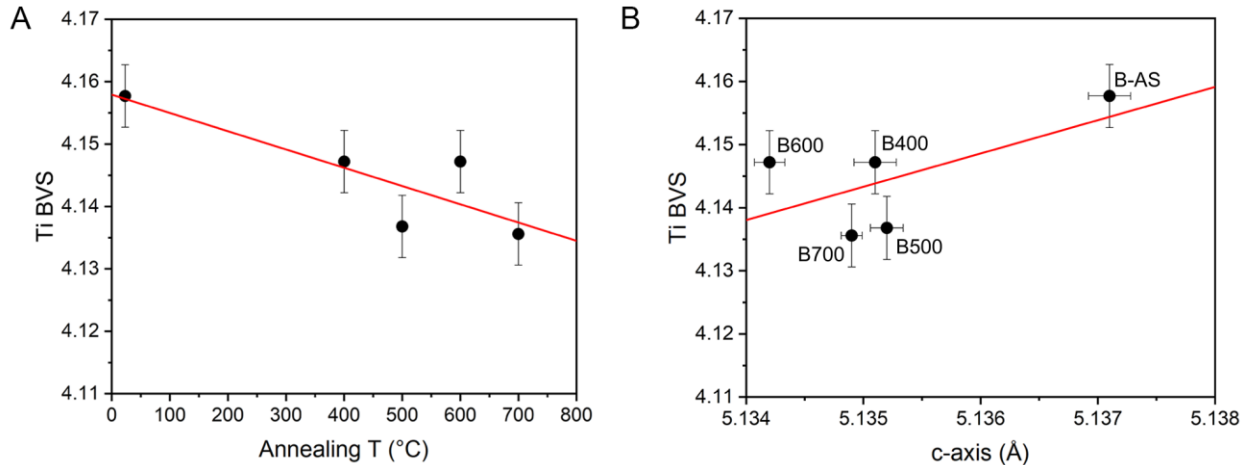
Note S4. Related to Figures S12–S19 and Table S3–S6. XRD analysis (Figure S12 and Table S4) revealed that the synthesized brookite is crystalline and stable up to 700°C. The sample treated at 800°C, instead, presented around 91 wt. % of rutile phase, while at 900°C almost all the rutile is transformed to the Magnéli phase Ti_9O_{17}. At 1000°C, the other Magnéli phases Ti_4O_7 in 94 wt.% and Ti_5O_9 in 6 wt.% were generated. The phase stability of commercial brookite is up to 700°C (similarly to the as synthesized brookite) and after that reduction at 800°C induced the complete conversion to rutile (Figure S13 and Table S5). The XRD pattern of as synthesized and reduced anatase (Figure S14) samples indicates that the as synthesized anatase photocatalysts are stable at up to 500°C, while almost full conversion to rutile is obtained at 700°C (Table S5). The average particle sizes obtained using the Scherrer method for commercial brookite and anatase samples are in good agreement with those retrieved from TEM micrographs analysis.

To investigate more in depth the structural modifications induced by the reduction treatment, we performed detailed Rietveld refinements for the samples treated up to 700°C (Figure S15). All of the patterns are well described by single phase of brookite TiO_2 and, within the resolution of our measurements, we did not detect any spurious crystalline phases.

Figure S16A and B shows the reduction temperature (T) dependence of the average particle size, D (nm), and the average strain as obtained using the Williamson-Hall method. We observed a clear decrease of D for T = 400°C followed by an increase of average particle size above this T. On the other hand, the average particle strain weakly decreases at T=400°C keeping roughly the same value at higher T. This phenomenon can be associated to particle sintering since the sudden aggregation of particle can result in an increase of D owing to relieve of intraparticle tension by decreasing the overall particle strain. This is confirmed by the annealing temperature evolution of component of empirical extension of anisotropic microstrain broadening tensor refined by Rietveld refinements (Figure S16C). Indeed, we note a progressive convergence of these parameters to the same values indicating that the evolution of Williamson-Hall strain is explained by the tendency to form more isotropic particle aggregates at high annealing temperature. This morphological observation agrees with the TEM micrographs of reduced brookite B700 (Figure S1B), which confirm that brookite nanorods tend to aggregate in isotropic agglomerates upon reduction. The tendency toward powder aggregation can also explain the disagreement between the average nanorod lengths detected by TEM, both before and after reduction, and the average particle size retrieved by Rietveld refinements.

Figure S16D shows the annealing temperature evolution of the refined lattice parameters. Orthorhombic strain is defined as:

$$\eta = \frac{2(a - b)}{(a + b)}$$

where *a* and *b* are the unit cell axes. We observed that η remains almost unchanged for all the investigated annealing temperature whereas the c-axis shows a clear decrease. In other words, this indicates that the annealing temperature does not affect the *ab* plane but induces distortion along the c-axis only. This anisotropic evolution of structural parameters upon reduction is even better outlined by the interatomic distances related to the TiO_6 octahedra. TiO_2 structure is composed of TiO_6 octahedra, each with a titanium atom at its center and oxygen atoms at its corners (Figure S17A). In brookite TiO_6 has distorted oxygen atoms in two different positions, namely O1, O2. This results in two groups of distances namely d_{Ti-O1}, d_{Ti-O2} (Figure S17B, C) which can be regrouped into two axial and four equatorial different interatomic distances which have been averaged out and shown in Figure S18. Averaged axial distance expands upon increasing temperature, whereas the average equatorial distances show a weak contraction. Both distances tend to the same value and this may indicate that the annealing process induces the TiO_6 to be more regular, i.e. isotropic, and less distorted at high temperature. To figure out the effect of reduction treatment on the brookite structure we argue that the reduction of TiO_2 at high temperature creates oxygen vacancies (V_O, in Kröger–Vink notation)[22,23] and induces Ti^{3+} ions electron trapped in Ti^{4+} lattice sites (Ti'_{Ti}) according to the following relation:

$$O_O^x + 2Ti_{Ti}^x + H_2 \rightarrow V_O^{\bullet\bullet} + 2Ti'_{Ti} + H_2O$$
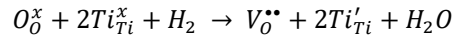
Two negatively charged Ti'_{Ti} species can then couple with one double positive charged $V_O^{\bullet\bullet}$ promoting the formation $< Ti'_{Ti} - V_O^{\bullet\bullet} - Ti'_{Ti} >$ defects. The mutual attraction between them can produce a contraction of the structure to account for electron neutrality, which is fully in agreement with the observed c-axis contraction upon reduction at high temperature. The reduction of Ti valence to produce Ti'_{Ti} species, is compatible with a depletion of $\approx -0.5\%$ as evidenced by bond BVS analysis, see for B700 (Figure S19A). Further, the correlation between the BVS and c-axis contraction is shown in Figure S19B, showing a nearly linear relationship between these two parameters and thus indicating that more $V_O s$ are induced by the reduction and more the c-axis resulted to be contracted. This highlights that reduction treatment introduced an anisotropic and preferential deformation of the brookite lattice along the c-axis.
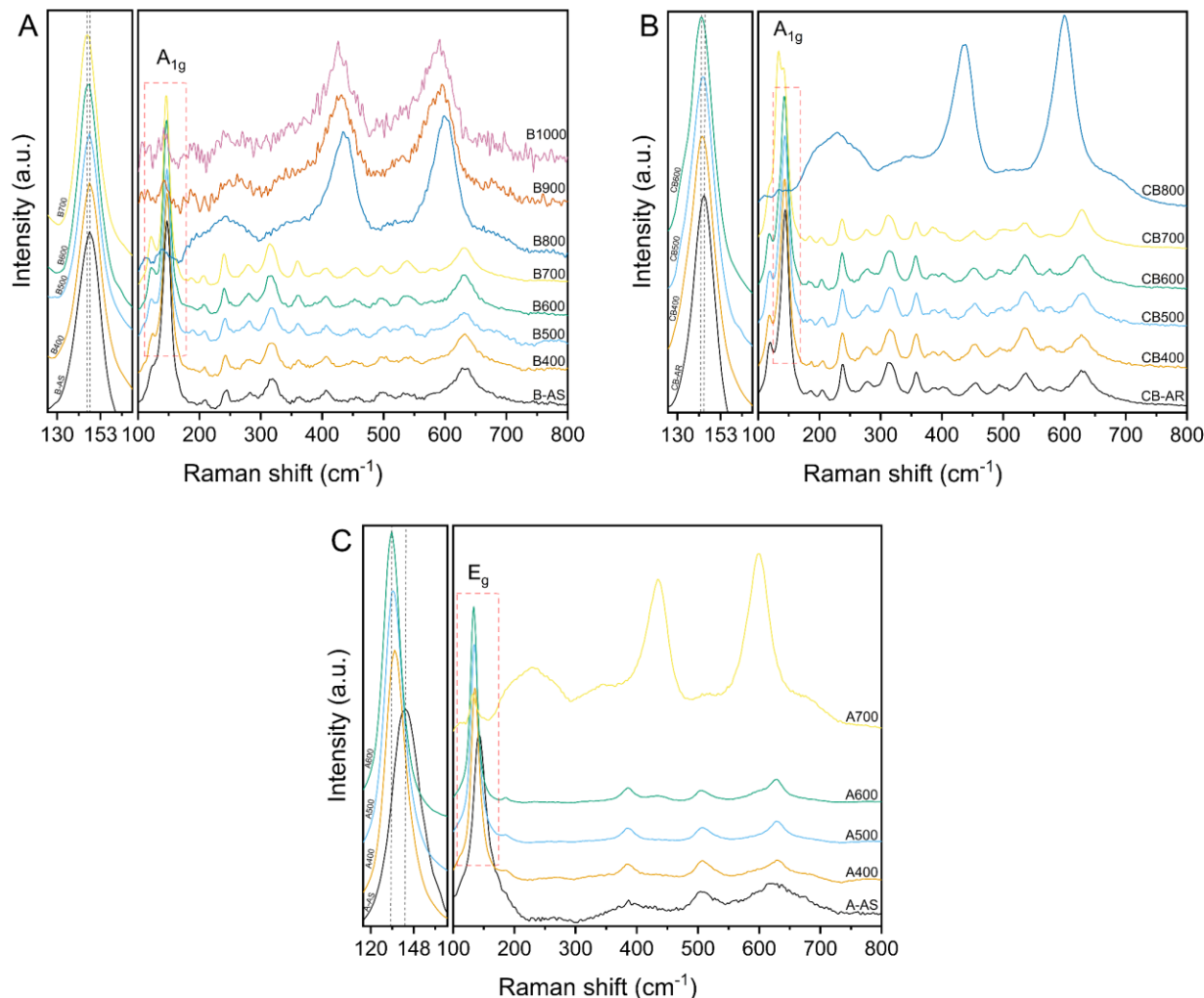
Figure S20. Raman spectra of TiO$_2$ samples. Raman spectra of (A) as-synthesized and reduced anisotropic brookite samples, (B) as-received and reduced commercial brookite samples, and (C) as-synthesized and reduced anatase samples. Measurements performed with a 455 nm laser at a power density of 0.1 mW cm^{-2}. The left part of each panel is the zoomed view of the main Raman peaks.

Note S5. Raman spectroscopy, related to Figure S20. The crystal system of brookite is orthorhombic and has eight formula units per unit cell and thirty-six Raman active modes $(9A_{1g}+9B_{1g}+9B_{2g}+9B_{3g})$[24]. The crystal system of anatase is tetragonal and has two formula units per unit cell and six Raman active modes $(A_{1g}+2B_{1g}+3E_g)$[24]. The crystal system of rutile is tetragonal and has two formula units per unit cell and four Raman active modes $(A_{1g}+B_{1g}+B_{2g}+E_g)$[24].

Raman spectra of as synthesized and reduced brookite samples (Figure S20A) confirmed that the synthesized brookite is stable up to 700°C and after that it transforms to rutile, as evidenced by the disappearance of brookite peaks and appearance of rutile peaks in Raman spectra of B700 and B800. The same Raman modes of rutile remained evident also for B900 and B1000, where an additional phase transition to Magnéli phases is completed. The main Raman peak of as synthesized brookite at 147.3 cm^{-1} is blue shifted to 146.0 cm^{-1} after reduction at 700°C. Moreover, there is a peak narrowing in the main peak due to the reduction (FWHM$_{B-AS}$ = 15.82 cm^{-1}, FWHM$_{B700}$ = 12.81 cm^{-1}).

Raman spectroscopy measurements also revealed that the commercial brookite sample is stable under reducing conditions up to 600°C, after which, rutile Raman fingerprint developed. There is almost no peak shift and no change in FWHM of the main peak (FWHM$_{CB-AR}$ = 16.41 cm^{-1}, FWHM$_{CB600}$ = 16.64 cm^{-1}) (Figure

S20B), suggesting that no significant modifications occurred in the commercial brookite lattice upon reduction at high temperature.

Figure S20C shows, instead, that anatase is stable up to 500°C in our reduction conditions showing also a significant blueshift of the main Raman mode from 142.2 cm^{-1} for as-synthesized anatase to 134.6 cm^{-1} for anatase reduced at 500°C. The same peak narrowed significantly from $FWHM_{A-AS}$ = 30.97 cm^{-1} to $FWHM_{A500}$ = 13.80 cm^{-1}.

Several phenomena can give rise to TiO_2 Raman peak shifting and broadening (or narrowing)[24–28] as follows: (i) the lattice strain[26], (ii) the crystal size that could regulate the phonon confinement and the Raman scattering (increasing in crystal size results in redshift and peak narrowing)[24], and (iii) the oxygen stoichiometry, depending on the phase of TiO_2, could affect the position of Raman peaks and could also modify the FWHM[25]. In the case of synthesized brookite and anatase, we observed a blueshift and peak narrowing of the main Raman peak after reduction. Upon reduction, we detected a reduction of lattice microstrain in brookite nanorods (Figure S20C) as well as an increase in the overall crystal size due to nanorods aggregation. Therefore, we propose that the change in oxygen stoichiometry (as also evidenced by the other characterizations reported) underlies the blue shift and the peak narrowing witnessed for both brookite and anatase[25]. In contrast, in case of commercial brookite neither peak shifting nor peak narrowing (or broadening) were observed. This result confirms that the commercial brookite was lightly reduced under reduction conditions as already suggested by UV-vis diffuse reflectance spectra analysis, TPR-MS measurements, and also by the color of the samples, which did not change upon reduction treatment (Table S1).
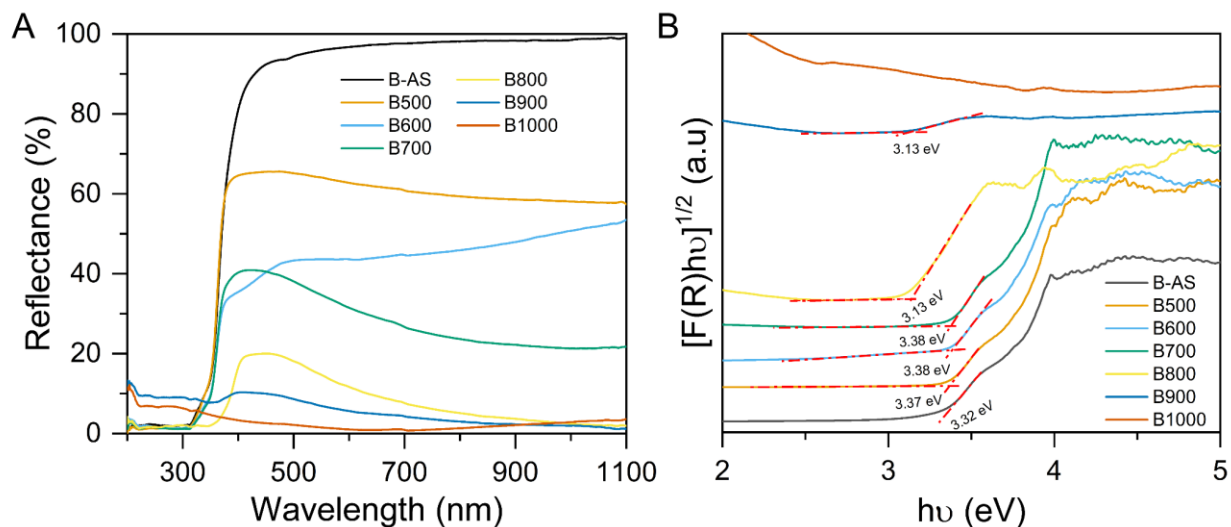

Figure S21. Diffusive reflectance data for brookite nanorods. (A) Diffusive reflectance spectra and (B) Tauc plots of as synthesized and reduced anisotropic brookite samples.
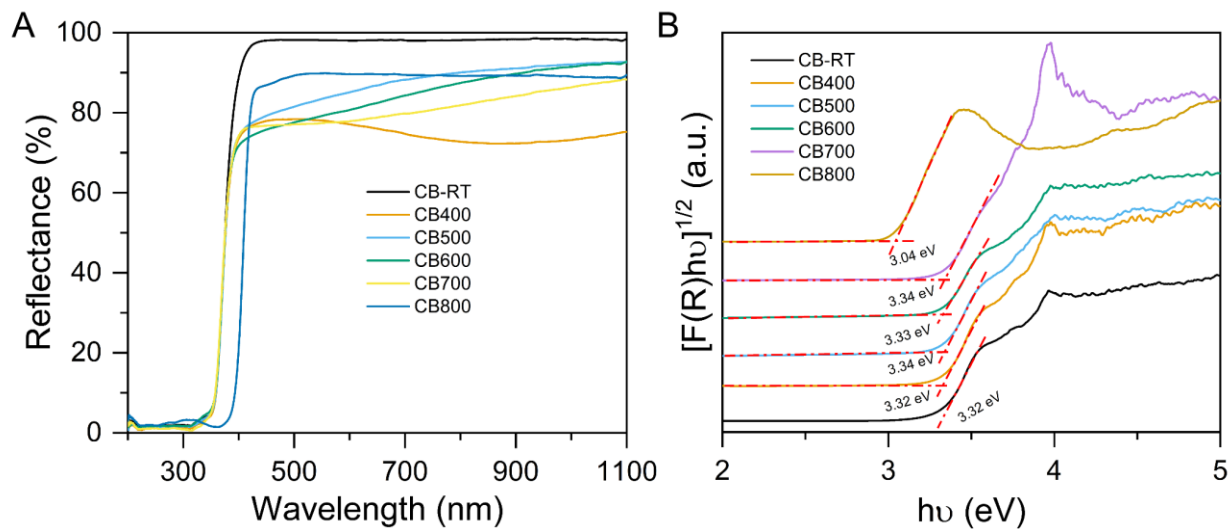
Figure S22. Diffusive reflectance data for commercial brookite. (A) Diffusive reflectance spectra and (B) Tauc plots of as received and reduced commercial brookite samples.
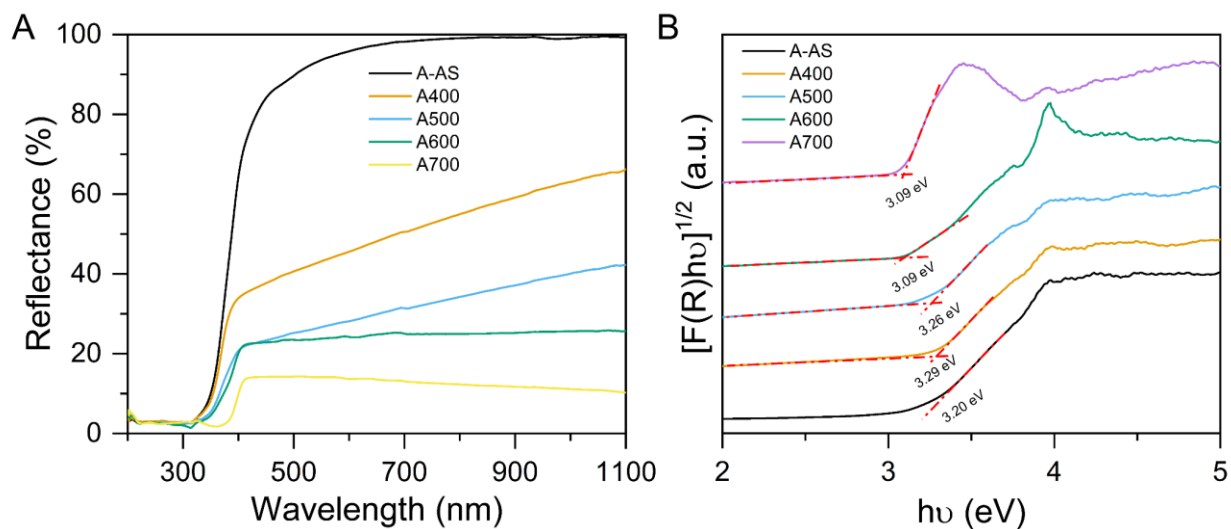

Figure S23. Diffusive reflectance data for anatase. (A) Diffusive reflectance spectra and (B) Tauc plots of as synthesized and reduced anatase samples.

Table S7. Bandgap values for brookite nanorods, related to Figure S21. Optical bandgap and Urbach energy of anisotropic brookite samples.

Sample	Optical bandgap (eV)	Urbach energy (meV)
B-AS	3.32	69
B500	3.37	67
B600	3.38	104
B700	3.38	115
B800	3.13	155
B900	3.13	-
B1000	-	-

Table S8. Bandgap values for commercial brookite, related to Figure S22. Optical bandgap and Urbach energy of commercial brookite samples.

Sample	Optical bandgap (eV)	Urbach energy (meV)
CB-AR	3.32	58
CB400	3.32	55
CB500	3.34	54
CB600	3.32	56
CB700	3.34	39
CB800	3.04	36

Table S9. **Bandgap values for anatase, related to Figure S23.** Optical bandgap and Urbach energy of anatase samples.

Sample	Optical bandgap (eV)	Urbach energy (meV)
A-AS	3.20	115
A400	3.29	154
A500	3.26	205
A600	3.09	252
A700	3.09	100

Note S6. Diffuse reflectance spectroscopy, related to Figure S21–S23 and Table S7–S9.
The Tauc method[29] is one of the most common procedures for determining the bandgap of materials. This method makes a relationship between absorption coefficient and optical bandgap of material based on the following formula:

$$(\alpha h v)^n = (h v - E_g)$$

where, α is the absorption coefficient, h is the Plank constant, v is the frequency of radiation, and E_g is the bandgap of material. The n factor depends on the nature of the electronic transitions and is equal to 2 for TiO_2 as it is an indirect bandgap semiconductor[30,31]. This method assumes that the scattering component of the reflected irradiation is zero. However, in case of nanopowders with high amount of scattering, this component could not be neglected. Therefore, the Kubelka-Munk theory is used to make an estimation of absorption from reflectance according to the following formula[32]:

$$F(R) = \alpha = \frac{K}{S} = \frac{(1-R)^2}{2R}$$

where, R is the reflectance of the sample with infinite thickness to avoid any contribution of substrate, K and S are the absorption and scattering coefficients, respectively. The bandgap of TiO_2 can be retrieved using the Tauc method as follows:

$$(F(R)h v)^{1/2} = (h v - E_g)$$

From the Tauc plot, the x-axis intersection point of the tangent to the linear increase of light absorption in the Tauc plot gives the band gap energy. This method is accurate and used here for determining the

bandgap energy of pristine TiO_2 materials, while for reduced TiO_2 powders the baseline method was employed to calculate the bandgap[32].

Furthermore, we analyzed the Urbach tail in absorption spectra, as it originates optical transitions involving intragap states related to defects[33–35]. The Urbach energy can be calculated as follow[36,37]:

$$\alpha = \alpha_0 + \exp(\frac{E}{E_u})$$

where α is the absorption coefficient, E is the photon energy equal to $h\nu$ and $\underline{E}_u$ is the Urbach energy, which can be retrieved by the reciprocal of the slope of the linear part of the curve.

Figure S21 shows the absorption spectra of as synthesized and reduced anisotropic brookite samples. As expected, most of the UV light is absorbed owing to the wide bandgap of brookite, which was found to be comprised between 3.32 and 3.36 eV (Table S7) for all samples containing only the brookite phase (B-AS, B500, B600, B700). A large shift in the absorption edge of B800 and B900 was observed due to the phase change to rutile, with a corresponding decrease of bandgap values around 3.1 eV. The sample B1000 absorbs almost the entire spectrum and it is not possible to calculate any bandgap. This can be ascribed to a phase composition including several semimetallic (Magnéli) phases[38]. The absorption of anisotropic brookite samples in the visible region increases by increasing the temperature of reduction, which is predictable from the color of powders, and it can be assigned to the introduction of oxygen vacancies and Ti^{3+} electronic states. However, visible light has no influence in the photocatalytic activity of the reduced brookite, as discussed in the photocatalysis section reported above. Furthermore, in all samples, a change in the Urbach tail due to the reduction at different temperatures was observed. It varied from 69 to 115 meV passing from B-AS to B700, suggesting an increased population of point defects in TiO_2.

Reflectance spectra for commercial brookite and synthesized anatase (with isotropic crystal shape) are reported in Figure S22 and Figure S23. In addition, Table S8 and

Table **S9** provides the results obtained from analysis of bandgap and Urbach energy of commercial brookite and anatase, respectively. It is clear that in all cases the bandgap underwent to a slight modification after reduction, remaining around 3.3 and 3.2 eV, for commercial brookite and anatase, respectively. After phase transformation to rutile (occurring at 800°C in commercial brookite and at 600°C in anatase), bandgap values decreased and Urbach energy increased. Furthermore, no change in color of the commercial brookite samples was observed after reduction at different temperatures (Table S1), while for anatase samples the color changed from white to gray and black. The variations of Urbach energy is in agreement with this observation: for commercial brookite it remained at a stable value of ~55 meV before and after reduction, while for anatase Urbach energy increased from 115 (A-AS) to 205 meV (A500). These results further confirmed that commercial brookite was hardly reducible, while defects could be introduced in the synthesized anatase.
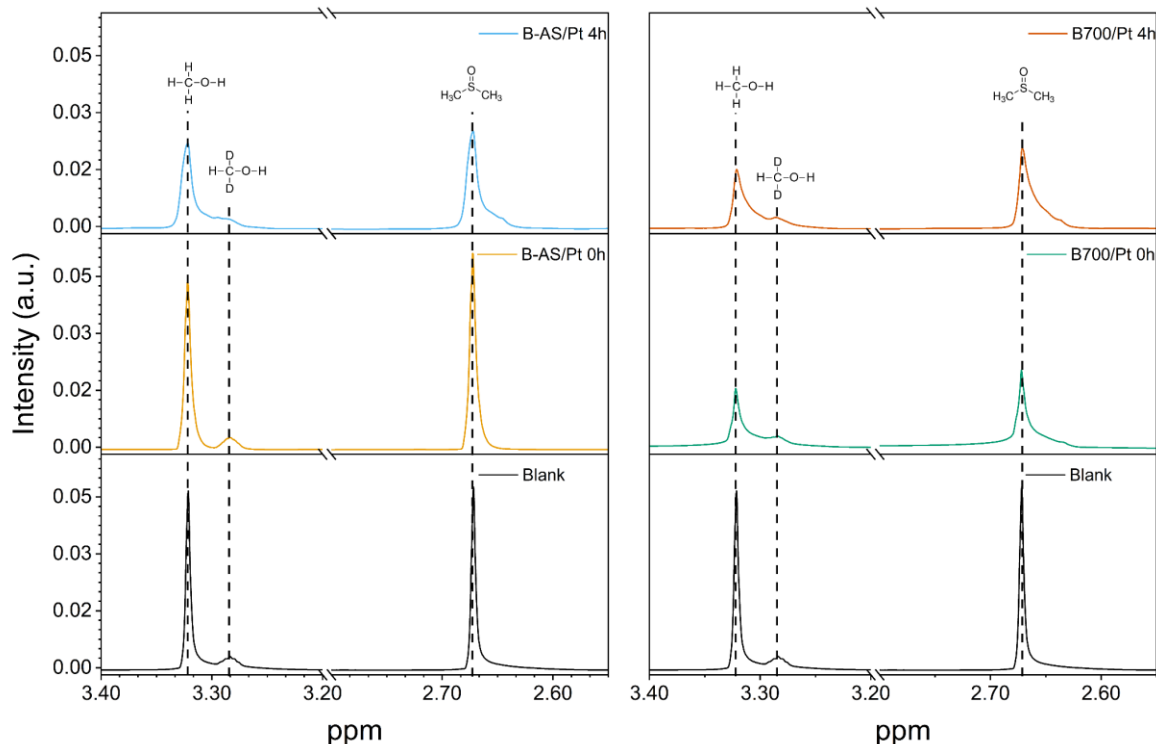
Figure S24. NMR analysis from methanol photoreforming, related to Figure 1. ^{1}H-NMR spectra of the solutions after photocatalysis at representative reaction times for B-AS/Pt and B700/Pt samples. The blank samples were recorded by using solutions containing CD_3OD, DI water, and DMSO ((CH_3)$_2$SO) as the internal standard. In the other samples, an aliquot of 50 µL of CH_3OH was added to the solution and its photocatalytic consumption rate was measured by assessing the area of its characteristic NMR peak. CHD_2OH is the impurity presents in the deuterated methanol.

Table S10. **NMR analysis from methanol photoreforming, related to Figure 1.** Relative NMR integration values of MeOH signal to internal standard (DMSO) at different reaction times for the pristine (B-AS/Pt) and reduced brookite (B700/Pt) samples.

Time (h)	B-AS/Pt	B700/Pt
-[a]	1.04[a]	0.92[a]
0[b]	1.03[b]	0.92[b]
2	1.03	0.88
4	1.02	0.85
6	1.02	0.83
8	1.01	0.83
10	1.02	0.82
16	0.99	0.78
24	0.96	0.75

[a]Blank measurements with no photocatalyst, but in the presence of the reagents *d4*-MeOH (5 mL), H_2O (5 mL), MeOH (50 µL), and DMSO (2 µL).
[b]Results were obtained after addition of the photocatalysts (B-AS-Pt and B700-Pt) to the solutions and stirring for 30 min in the absence of light to allow for reaching the adsorption/desorption equilibrium.
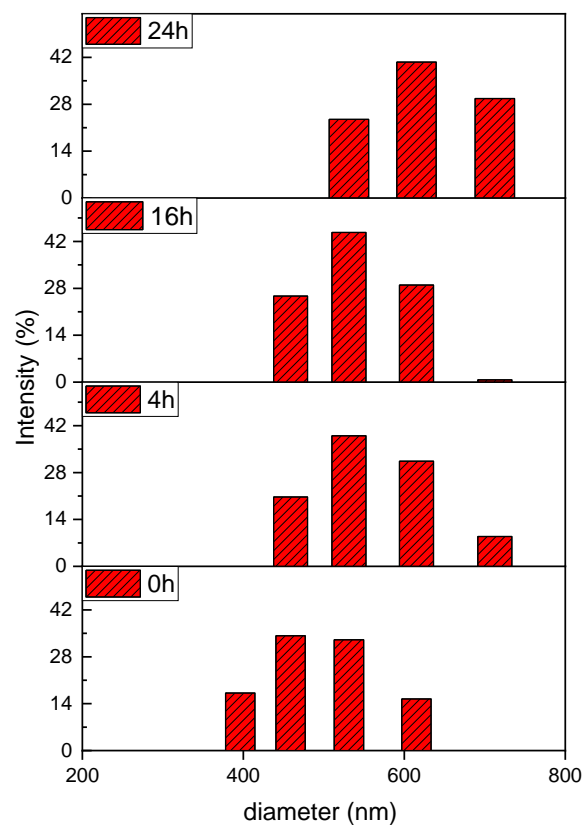
Figure S25. Stability of colloidal photocatalysts under irradiation. Dynamic Light Scattering (DLS) measurements analysis showing the hydrodynamic diameter evolution of the B700/Pt catalysts during the reaction.
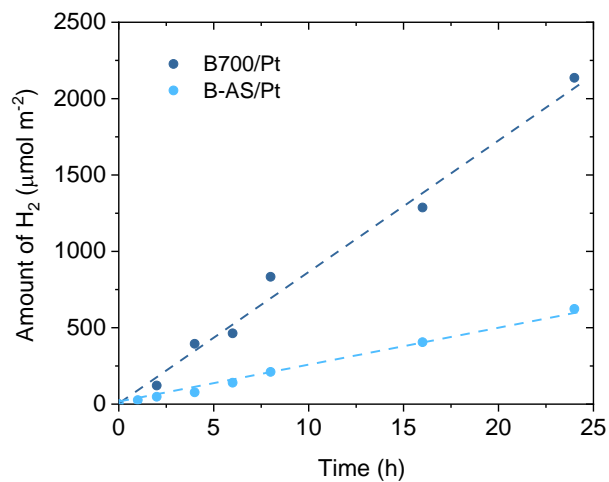

Figure S26. Hydrogen evolution kinetics, related to Figure 1. Hydrogen evolution kinetics for B-AS/Pt and B700/Pt under one Sun illumination.
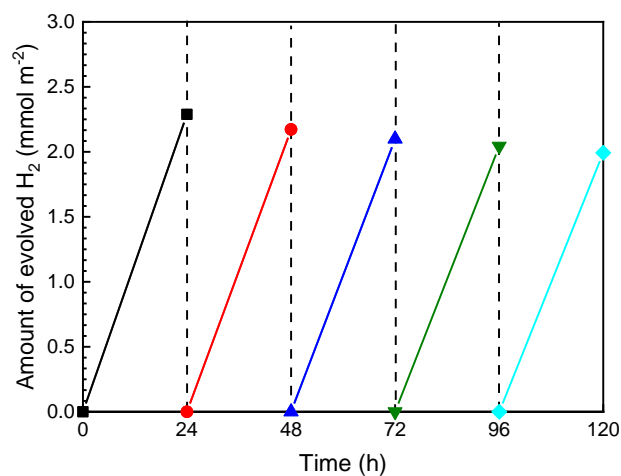
Figure S27. **Hydrogen evolution stability, related to Figure 1.** Hydrogen amount evolved from five consecutive photocatalytic cycles for B700/Pt during methanol photoreforming under one Sun illumination.
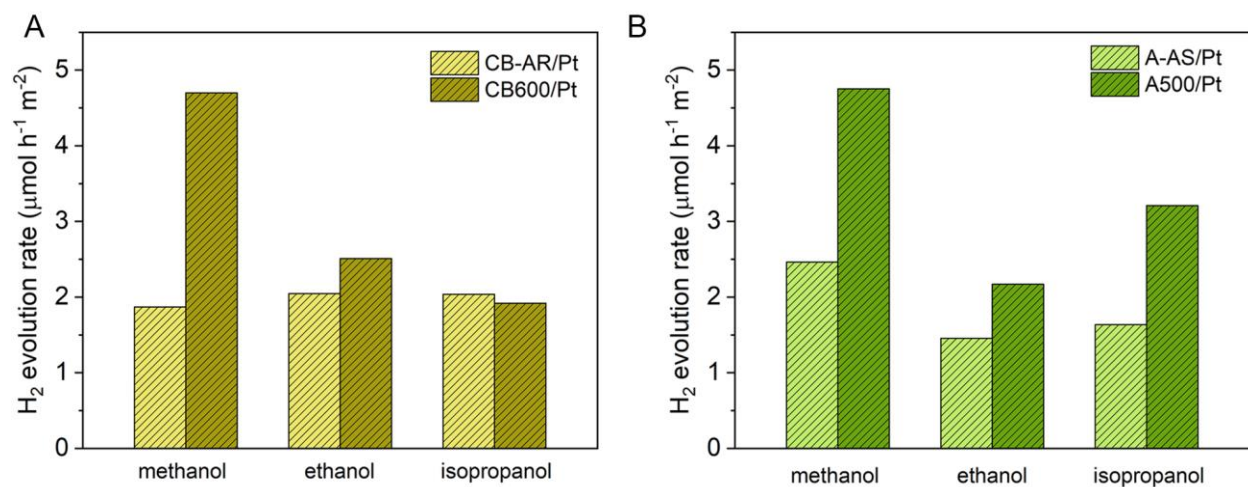

Figure S28. Hydrogen evolution activity with different alcohols, related to Figure 1. Specific hydrogen evolution rate during methanol, ethanol, and isopropanol photoreforming obtained for samples loaded with 1 wt.% Pt by normalizing the photocatalytic rates by BET specific surface area for (A) pristine (CB-AR/Pt) and the most active reduced commercial brookite (CB600/Pt), and (B) for as-synthesized (A-AS/Pt) and the most active reduced anatase (A500/Pt).
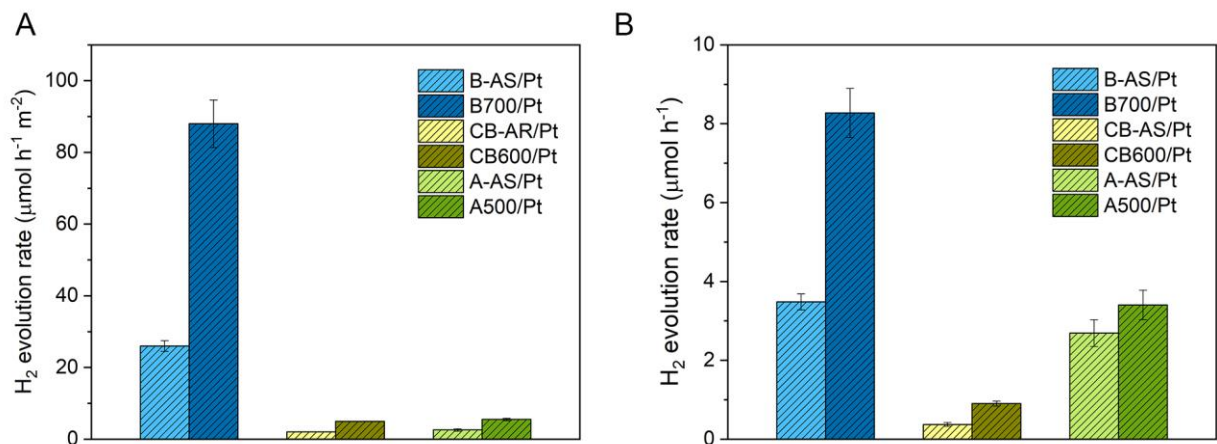
Figure S29. Hydrogen evolution activity with different normalization, related to Figure 1. (A) Specific hydrogen evolution rate obtained for samples loaded with 1 wt.% Pt by normalizing the photocatalytic rates by BET specific surface area (per optimized mass) for pristine (B-AS/Pt) and the most active reduced brookite nanorods (B700/Pt), as-received (CB-AR/Pt) and the most active reduced commercial brookite (CB600/Pt), as-synthesized (A-AS/Pt) and the most active reduced anatase (A500/Pt). (B) Hydrogen evolution rate per optimized mass for the same samples reported in A.
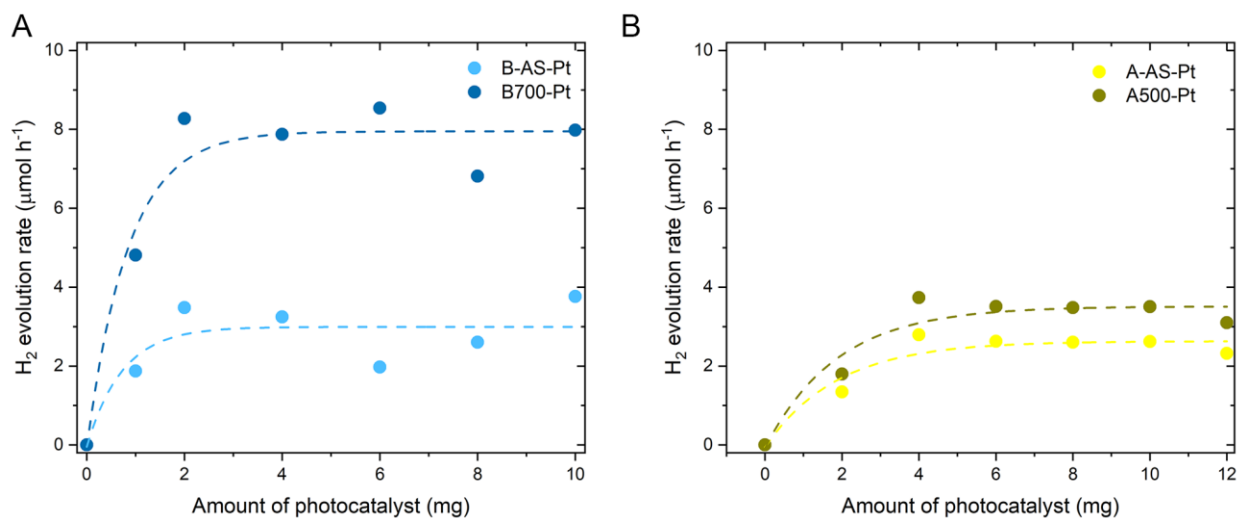

Figure S30. Mass optimization for different photocatalysts, related to Figure 1. Photocatalytic hydrogen evolution rate optimized per mass of used photocatalyst for (A) for B-AS/Pt and B700/Pt; (B) A-AS/Pt and A500/Pt under one Sun illumination.
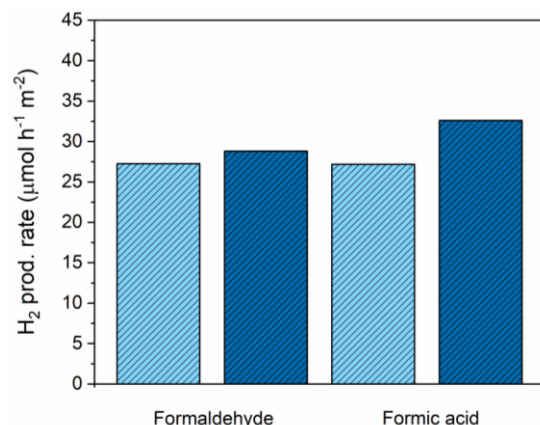
Figure S31. Hydrogen generation from reaction intermediates, related to Figure 1. (A) Hydrogen production rate from different intermediates of methanol oxidation (formaldehyde and formic acid) of as-synthesized (light blue) and reduced at 700°C (dark blue) brookite samples loaded with 1 wt.% Pt. These experiments confirmed GC analysis of the gas phase (i.e., we detected only carbon dioxide) and NMR analysis of the liquid phase after reaction (i.e. we did not detect any signal related to formaldehyde nor formic acid) indicating that the methanol photo-oxidation proceeded to carbon dioxide, due to reactivity of brookite nanorods toward oxidation of the intermediates (formaldehyde and formic acid) of methanol oxidation. Photolysis of formaldehyde under AM 1.5G one Sun illumination produced a very small hydrogen production rate, namely, ~85 nmol m^{-2} h^{-1}.
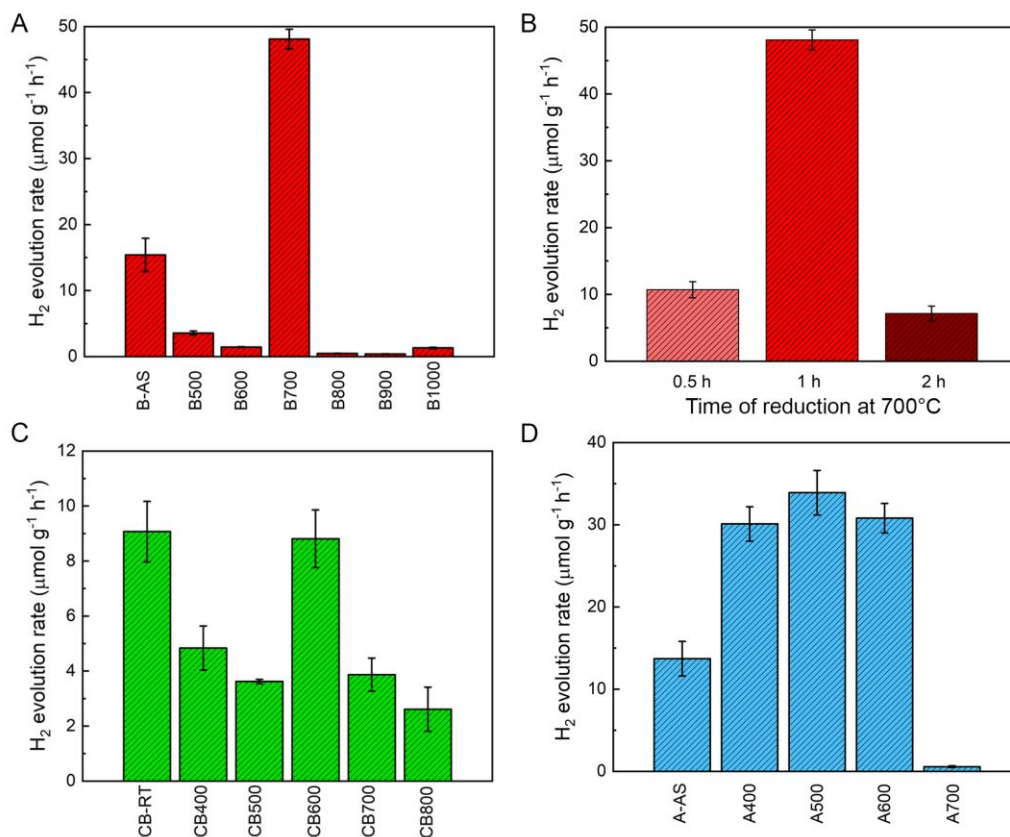

Figure S32. Hydrogen activity optimization for the samples with no Pt loading, related to Figure 1. Co-catalyst free rate of hydrogen evolution of TiO_2 samples tested under one Sun illumination for 24 h and reduced under pure hydrogen for 1 h: (A) brookite nanorods, (B) brookite nanorods reduced at 700°C for different times, (C) commercial brookite, and (D) synthesized anatase. We report the specific H_2 evolution rate only for the most performing platinized sample for each series in Figure S29.
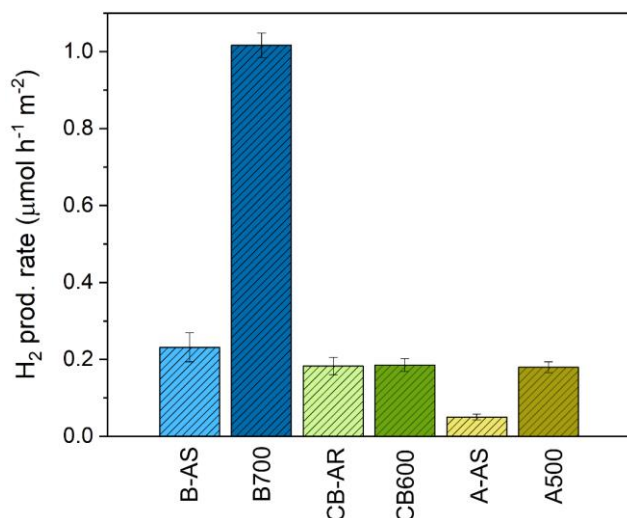
Figure S33. Hydrogen generation from the best samples with no Pt loading, related to Figure 1. Specific hydrogen evolution rate obtained by normalizing the photocatalytic rates by BET specific surface area for as-synthesized (B-AS) and the most active reduced brookite (B700), as-received (CB-AR) and the most active reduced commercial brookite (CB600), and as-synthesized (A-AS) and the most active reduced anatase (A500).

Note S7. Methanol photoreforming, related to Figure S24–S31 and Figure 1. In order to demonstrate the better photo-oxidation acitivty toward methanol of reduced brookite, we performed a series of photocatalytic experiments detecting (1) the methanol consumption rate through ^{1}H-NMR spectroscopy and (2) the hydrogen evolution rate with GC for platinized B-AS and B700. We did not detect any trace of formaldehyde nor formic acid in both liquid phase (through NMR analysis) and gas phase (through GC analysis), suggesting that methanol oxidation proceeded toward CO_2, as confimed by the high reactivity of brookite samples toward the oxidation of formaldehyde and formic acid solutions (Figure S31).

The specific photocatalytic H_2 evolution rates expressed in μmol m^{-2} h^{-1} shown in Figure S29 underly that nanorods of reduced brookite (B700) have a specific photocatalytic activity that is 4.4-, 5.6-, and 5.7-fold the ones of as synthesized brookite (B-AS), reduced commercial brookite (CB600), and reduced anatase (A500), respectively. These results demonstrate that higly active sites for photocatalysis are formed in B700 upon reduction under hydrogen atmosphere. Interestingly, when we performed H_2 evolution experiments with B700 in H_2O/methanol under one Sun light irradiation and applying a longpass optical filter to cutoff $\lambda \geq 380$ nm, i.e. cutting optical excitation above bandgap energy, we did not detect any H_2 after 24 h of reaction. This finding suggests that the intragap electronic states due to the introduction of defects in TiO_2 upon reduction (see materials characterization and DFT calculations below) do not directly participate to the visible light photocatalytic activity in the H_2 evolution reaction. Further, experiments performed under one Sun illumination and using Na_2S (0.1 M) instead of methanol as a hole scavanger, did not produce any H_2 suggesting that the H_2 evolution activity of our reduced brookite is regulated by its selective methanol photo-oxidation ability.
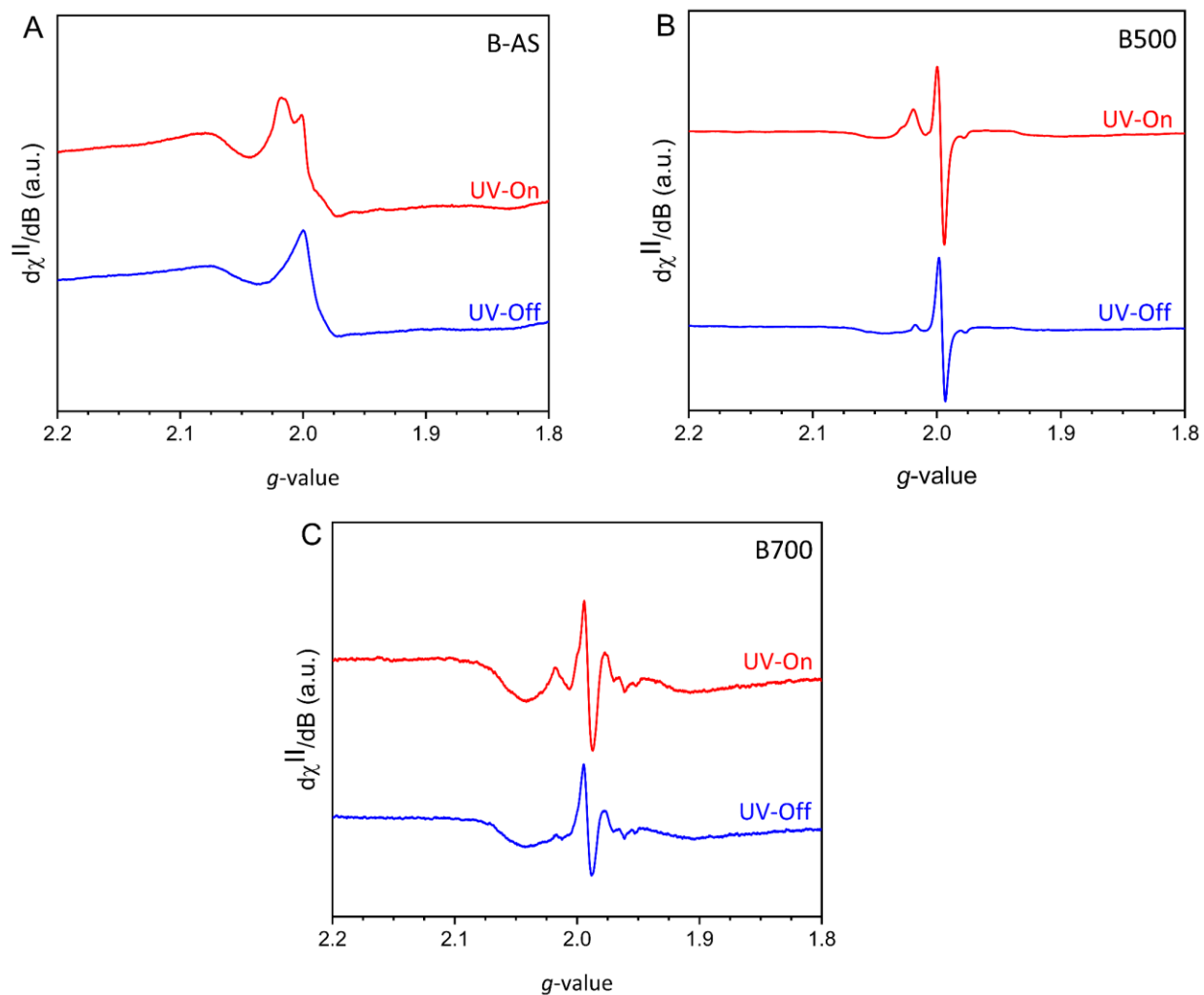
Figure S34. Electron spin resonance spectra of dry powders. X-band EPR spectra (9.1 GHz, T = 77 K) of (A) B-AS, (B) B500, and (C) B-700 recorded in powder form and measured in dark (blue lines) and under UV irradiation (red lines).
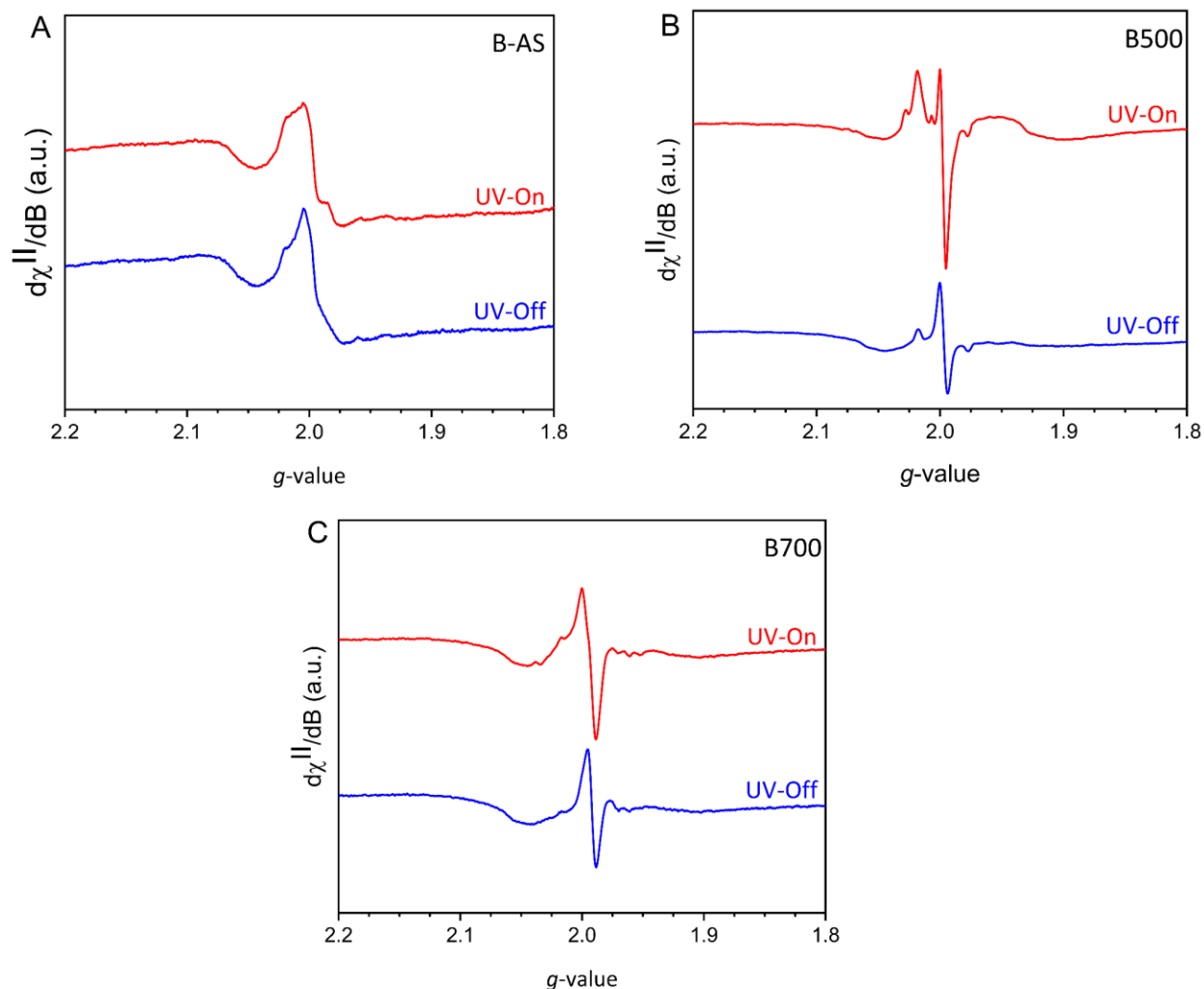
Figure S35. Electron spin resonance spectra of powders under in situ conditions. X-band EPR spectra (9.1 GHz, T = 77 K) of three samples studied (A) B-AS, (B) B500, and (C) B700 dispersed in the frozen solution of DI water and methanol (1:1, volume ratio) recorded in dark (blue lines) and under UV irradiation (red lines).
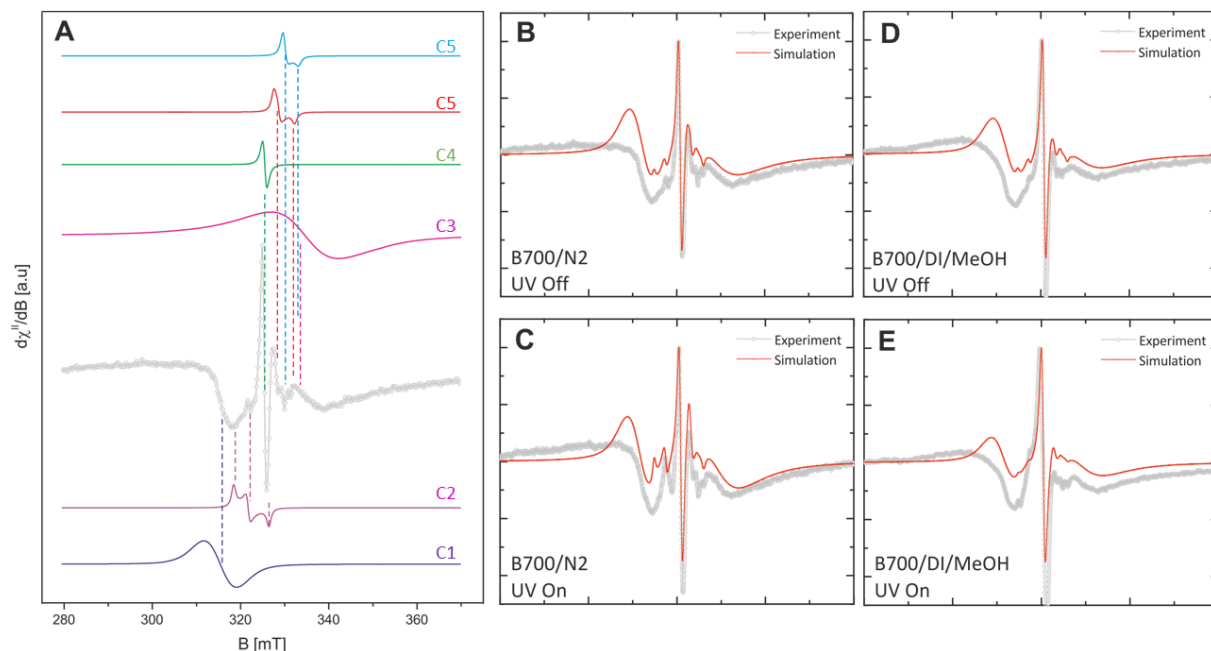
Figure S36. Electron spin resonance spectra and simulations. (A) an illustrative EPR envelope of B700 in contact with N_2 at 80K (grey spectrum) together with individual components (C1-C6) derived from simulation and discussed below, (B-E) comparisons of EPR spectra of B700 recorded in different conditions together with theoretically proposed model.

Note S8. Electron paramagnetic resonance spectroscopy, related to Figure S34–S36. In order to identify the nature of spin containing sites and their contribution to photocatalysis we used electron paramagnetic resonance (EPR) spectroscopy. Three samples have been tested, which differ in the annealing temperature in hydrogen atmosphere, B-AS, B500, and B700. We investigated these samples in powder form and in situ under photocatalytic conditions by using a water/methanol (MeOH) matrix.

The EPR spectrum of B-AS in powder form shown in Figure S34A exhibits a broad resonance, centered at $g \sim 2.0$. This signal arises from delocalized defects and presence of significant strains in the crystalline lattice, due to the synthetic procedure pursued. Following irradiation, a new resonant line appears in the spectrum, around $g = 2.017$. This signal originates from holes/oxygen-based radicals. From the double integration of the EPR signal recorded in light and dark conditions, we calculated an increase of about 25.6% in the total number of spin contacting sites after illumination. The observed increase in spin concentration indicates that fast electron/hole recombination processes are here hindered; thus, the photogenerated states are rather stable.

The EPR trace of B500 in powder form, on the contrary, is very strong and it is dominated by a sharp resonant line at g=1.997 (Figure S34B). This resonance arises from localized lattice embedded Ti^{3+} sites in an octahedral field. Upon UV irradiation, we witness an increase of the signal in the region of the spectrum associated to oxygen-based radicals at g=2.017. In this case, the double integrated EPR signal shows after UV light exposure an increase in the total number of spins of 13.7%. Therefore, the photoexcited states are here less stable than in B-RT and fast e^-/h^+ recombination processes occur in this sample.

The sample B700 in powder form in the dark (Figure S34C) gives a weaker EPR signal compared to B500, although being qualitatively similar. The major difference between B700 and B500 appears, in the former, to be linked with a larger distribution in crystal field strain (octahedral to rhombic) associated to the Ti^{3+} spins due to structural defects. Upon UV irradiation, an increase of 56.6% in spin concentration was observed. This behavior is interpreted as due to the high stability of photoexcited states and slow recombination processes in the material, i.e. in B700 in powder form we observed the highest increase of paramagnetic species accumulating under irradiation.

It is worthy to point out that the most efficient sample in hydrogen production and methanol consumption is B700, which gives indeed the weakest intensity in the EPR powder spectrum among the series here shown. Therefore, the number of spins recorded by EPR do not directly correlate with the system reactivity and its overall efficiency in the catalytic process.

To unveil in more detail the reasons underlying the different efficiency in the hydrogen production recorded in this series of tested materials, we performed a set of experiments under in situ photocatalytic conditions. In our experiments, 10 mg of materials were dispersed in 100 µL of solution of deionized (DI) water and MeOH (50:50). Under dark conditions the EPR fingerprints in frozen solutions of B-AS, B500, and B700 (Figure S35) appear very similar to those observed in their correspondent powder forms in contact with N_2. However, upon irradiation, significant differences in the ability of MeOH molecules to quench the photogenerated holes emerged. In particular, while in B-AS and B700 the interaction of MeOH molecules with photogenerated h^+ seems more effective, in B500 is not, as validated from the appearance of a strong peak at g=2.017 associated to accumulation of holes. Therefore, the decreased catalytic efficiency of B500 compared to B-AS and B700 arises from combination of two factors, i) fast electron/hole quenching during photoexcitation and ii) when holes are formed they do not tend to react with MeOH molecules, which translates into a lower probability of successful delivery of electrons for hydrogen production. From time-resolved PL measurements, however, the average lifetime of charge carriers is similar for both B500 (1.9 ns) and B700 (2.0 ns), suggesting how the reaction between holes and methanol is a determining factor addressing the photocatalytic activity trend.

The simulation and deconvolution of EPR spectra for samples B700 in light and dark conditions in contact with N_2 (in powder form) and DI water: MeOH (1:1, volume ratio) at 80K is shown in Figure S36. By deconvolution of EPR spectra we simulated the possible model of paramagnetic species present in the sample B700, which can be applied on all related spectra just by varying the proportions of individual components. We assigned five main species commented below.

Component C1: g=2.059 related to peroxyl radicals (Ti-O-O$^\bullet$) on the surface.

Component C2: S=1/2 system associated with a trapped hole (O-centre) in the lattice with g_x=2.038, g_y=2.017 and g_z=1.999.

Component C3: surface exposed Ti^{3+} centres which are highly disordered, and which give wide resonant line at g=1.935.

Component C4: sharp isotropic signal at g=1.992, we assume that this signal is associated with interstitial Ti^{3+} sides in pseudo octahedral positions.

Component C5: typical axial signal arising from Ti^{3+} in regular lattice positions with $g_{x,y}$=1.978 and g_z=1.952.

Component C6: Ti^{3+} in the lattice located in some sublayer under the surface, where are lattice parameters slightly shortened and therefore g value is smaller comparing to C5, to be precise $g_{x,y}$=1.963 and g_z=1.944.
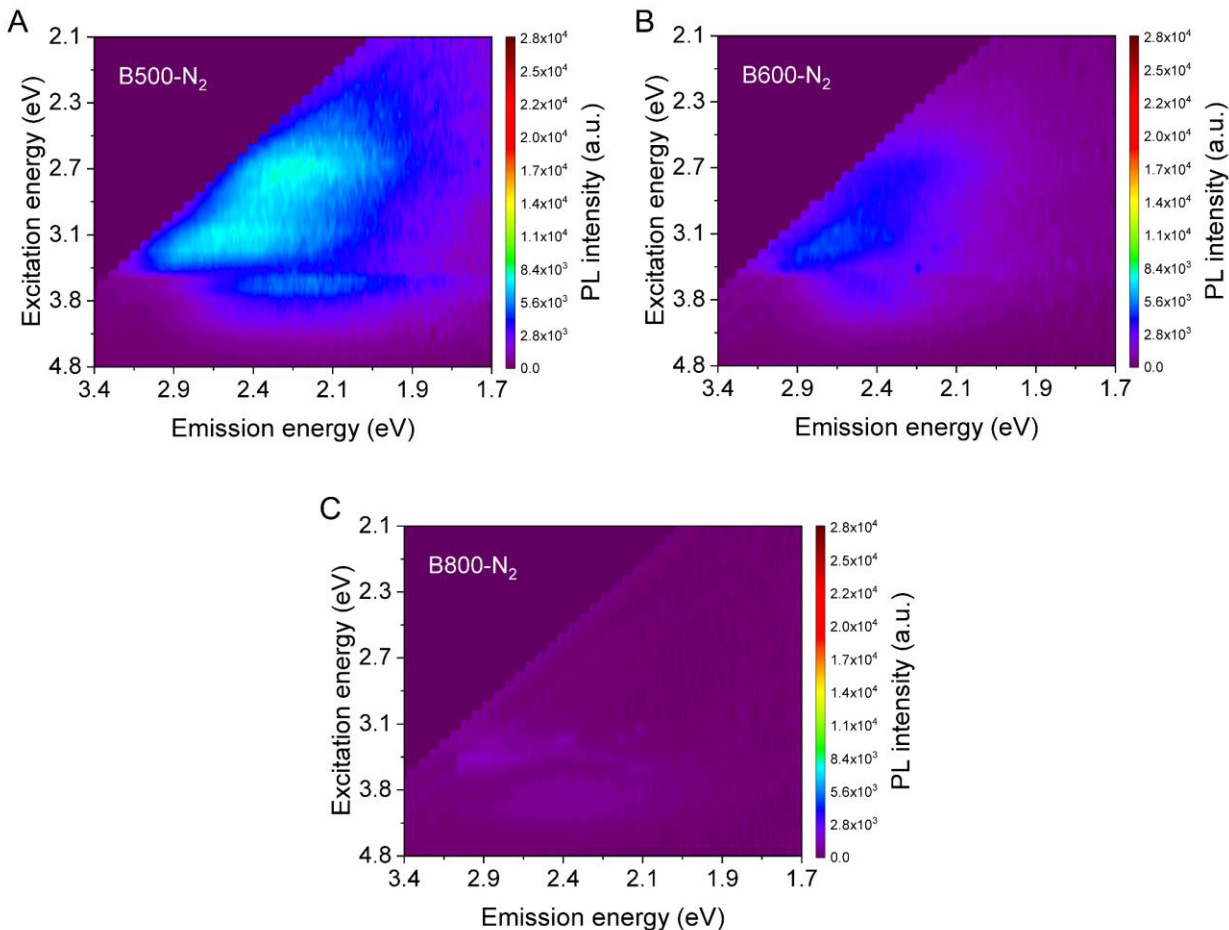
Figure S37. PL maps for reduced brookite nanorods, related to Figure 2. PL maps for (A) B500, (B) B600, and (C) B800. The measurement temperature was 80 K under N_2 atmosphere.
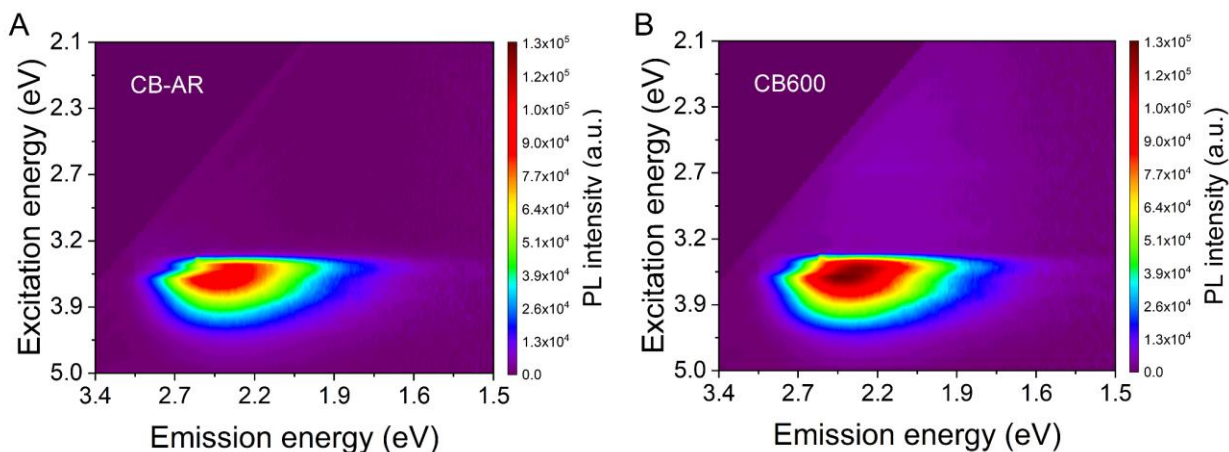

Figure S38. PL maps for reduced commercial brookite, related to Figure 2. PL maps for (A) as-received commercial brookite and (B) reduced commercial brookite at 600°C. The measurement temperature was 80 K under N_2 atmosphere.
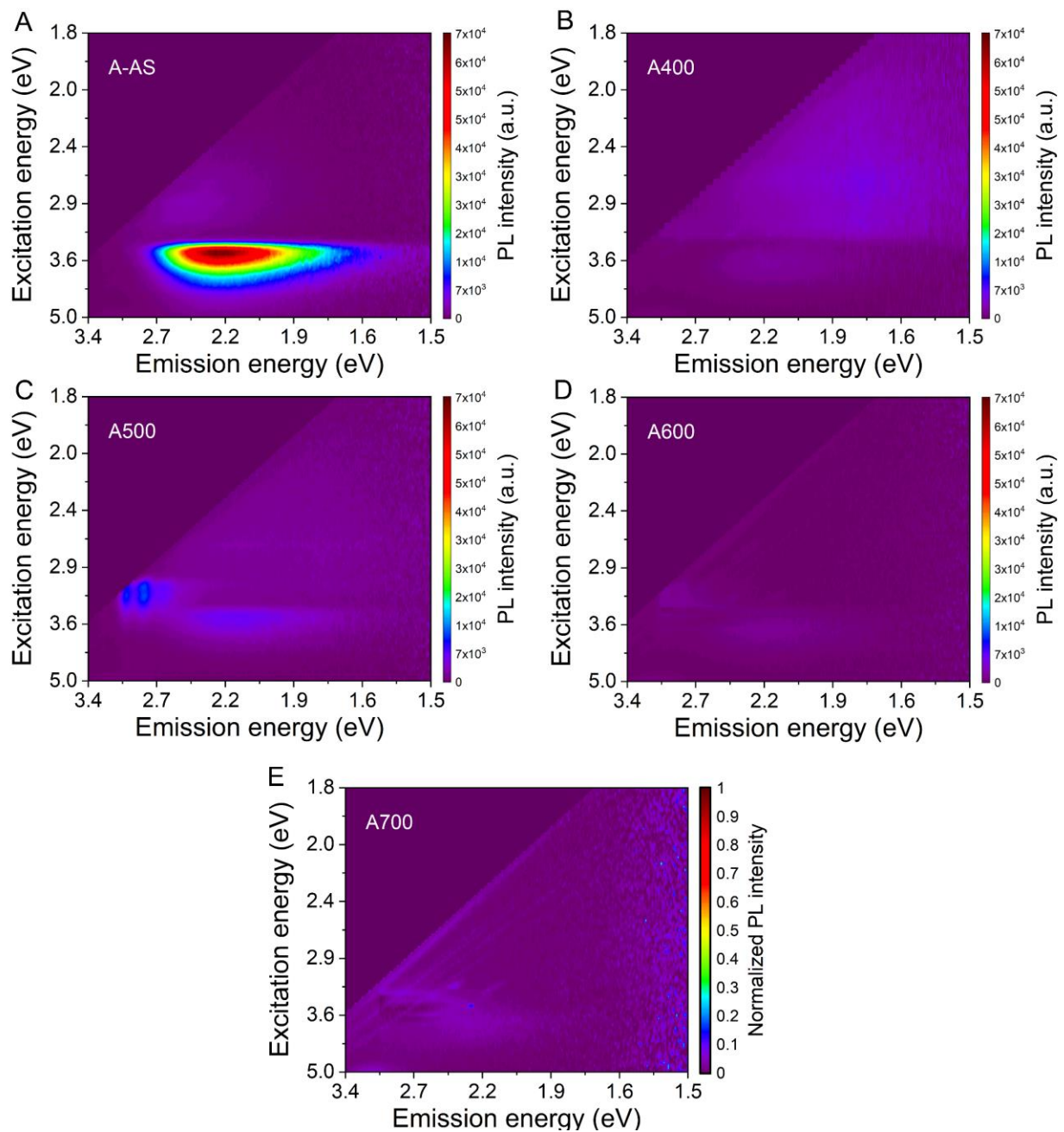
Figure S39. PL maps for reduced anatase, related to Figure 2. PL maps for (A) as-synthesized anatase, and reduced anatase at (B) 400°C, (B) 500°C, (B) 600°C, and (B) 700°C. The measurement temperature was 80 K under N_2 atmosphere.
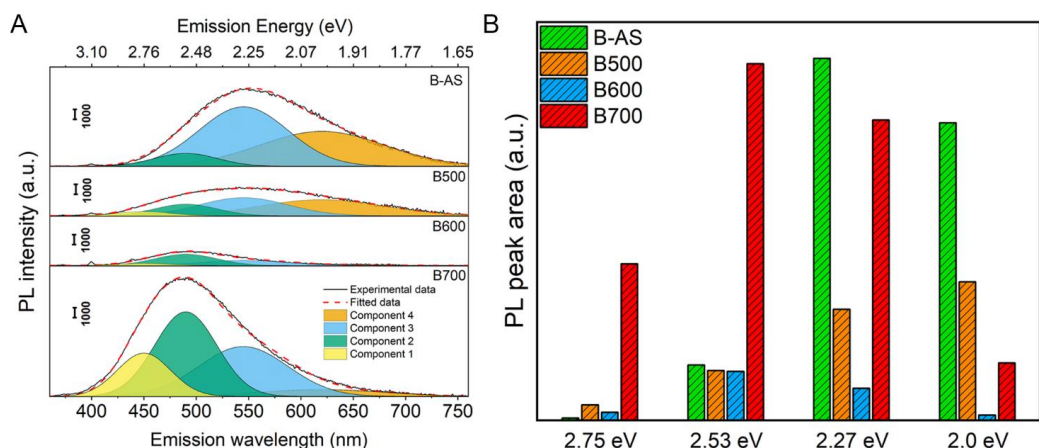
Figure S40. PL spectra for brookite nanorods, related to Figure 2. (A) Deconvoluted PL spectra for as-synthesized and reduced brookite samples, using an excitation energy 3.6 eV. (B) PL peak area related to each component retrieved from deconvolution and centered at 2, 2.27, 2.53, 2.75 eV. Both peak energy and width of each component were kept constant in each sample.
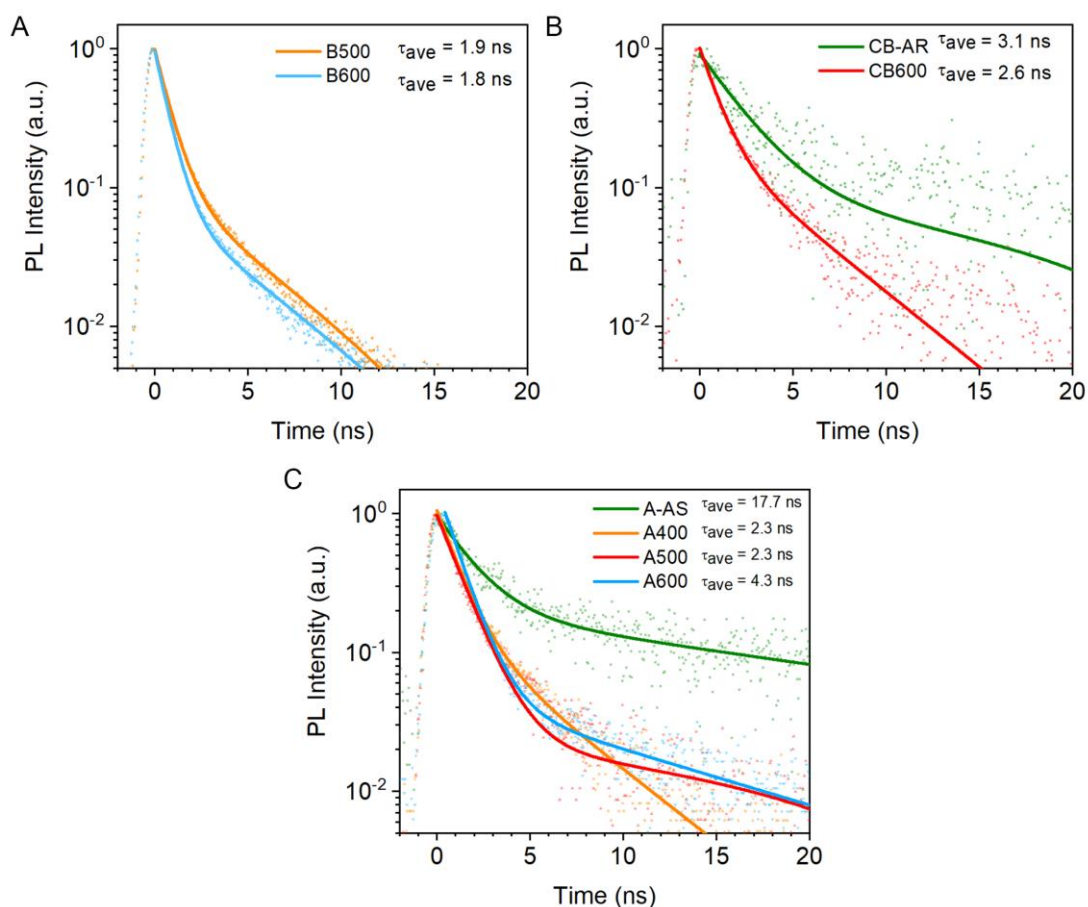
Figure S41. Time–resolved photoluminescence spectra for relevant investigated samples, related to Figure2. Time–resolved photoluminescence spectra of (A) brookite reduced at 500°C and 600°C, (B) as-received and reduced commercial brookite at 600°C, and (C) as-synthesized and reduced anatase at 400, 500, and 600°C. The dots are experimental data and the solid lines are the fitted curve. The τ_{ave} is the average electron lifetime extracted from the fitting.

Table S11. Lifetimes from PL measurements, related to Figure 2 and Figure S41. Time–resolved photoluminescence fitted parameters for as-synthesized (as-received) and reduced samples at different temperatures.

Sample	B_1, %	τ_1, ns	B_2, %	τ_2, ns	τ_{ave}, ns
B-AS	85	1.2	15	8.6	5.3
B500	87	0.7	13	3.6	1.9
B600	91	0.6	9	3.7	1.8
B700	90	0.8	10	4.0	2.0
A-AS	80.2	1.8	19.8	22.7	17.7
A400	85.1	1.1	14.9	4.1	2.3
A500	84.7	0.9	15.3	4.1	2.3
A600	95.4	1.0	4.6	10.8	4.3
CB-AR	100.0	3.1	-	-	3.1
CB600	77.1	0.9	22.9	3.9	2.6

Note S9. Photoluminescence (PL) and time-resolved photoluminescence (TRPL) spectroscopy, related to Figure S37–S41, Table S11, and Figure 2 and 3.

Photoluminescence spectroscopy is a powerful technique for studying the radiative recombination of electrons and holes that populate intragap energy positions and that are due to the presence of structural defects in semiconducting materials[39]. Photoluminescence spectroscopy is often used in the literature to reconcile charge carrier recombination phenomena occurring in TiO_2 and its photocatalytic activity[40–42]. At first approximation, a higher PL intensity and lower PL lifetime underlie a higher electron and hole recombination rate and consequently a lower photocatalytic activity. However, the way radiative recombination processes may bring insight to photocatalytic activity also relates to: (i) the position of structural defects into the TiO_2 lattice (i.e. surface, subsurface, bulk) that, in turn, influences the energy distribution of electronic states due to defects (and therefore also the energy distribution of PL spectra), and (ii) how PL intensity and energy distribution change upon exposure to molecules employed in the photocatalytic tests as a hole scavenger (i.e. methanol).

To examine the luminescence behavior of our TiO_2 samples, we measured PL map spectra using several excitation wavelengths from 258 to 590 nm (4.8 eV down to 2.1 eV) and monitoring PL emission in the energy range from 364 to 730 nm (3.4 eV down to 1.7 eV). The samples were measured initially in the solid state at the temperature 80 K in contact with N_2 atmosphere. The PL maps for as synthesized brookite and B700 (the most active photocatalyst) are reported in the main text (Figure 2), while PL maps for B500, B600 and B800 are illustrated in Figure S37. From these PL maps, it is evident that PL intensity and energy distribution changed in each sample depending on the reduction temperature, suggesting that recombination centers (i.e. defects) re-organized and moved within the brookite lattice upon reduction at increasing temperatures[23,43]. A similar phenomenon was observed for each set of samples investigated, namely commercial brookite (Figure S38) and anatase (Figure S39). Within the synthesized brookite series, the most intense PL signal was recorded for B700 ≈ B-AS > B500 > B600 > B800. According to the XRD results, the sample B800 is already transformed to rutile phase and for this reason show a very weak PL in the investigated emission energy range. It is interesting to note that B-AS presents PL signal only when excited with above-bandgap photons, while B700 highlights a complex PL signal even for below-bandgap excitations, demonstrating that reduction modified the electronic structure of reduced brookite. In order to investigate more in depth this aspect, we deconvoluted the PL spectra of synthesized and reduced brookite (Figure S40) obtained using an excitation wavelength 340 nm (3.6 eV, above-bandgap). The spectra were fitted by 4 components peaking at 450, 490, 545 and 620 nm (2.75, 2.53, 2.27 and 2.0 eV, respectively). In each case, the peak position and the full width at half maximum (FWHM) of the deconvoluted peaks were kept the same and just the intensity of peaks was free to change.

Generally, it has been shown that anatase and brookite exhibit distinct PL bands in the visible region of the electromagnetic spectrum[44]. The well-accepted interpretative model[39] for these emissions include the presence of the main visible emission is composed of a green component ("type 1 PL" or "green PL"), at higher energies, due to recombinations between shallowly trapped electrons (or conduction band electrons) and deeply trapped holes, and a red component ("type 2 PL" or "red PL"), at lower energies, due to recombinations between valence band holes and deeply trapped electrons[45–49]. Spectra deconvolution reported in Figure S40 show that the weight of different PL components in our brookite samples significantly changes upon treatment in hydrogen at increasing temperatures. Importantly, the most intense PL components for B-AS are those at 2 and 2.27 eV, while for B700 (i.e. the most active photocatalyst), the higher energies PL components become dominant. The experimentally determined valence band photoemission spectra recorded at synchrotron using photon energy in resonance with the titanium x-ray absorption edge (Figure 3A in the main text) show that in case of B-AS, the native oxygen vacancies present in the brookite induced a distribution of intragap states acting as deep electronic traps, while for B700 a more defective structure induced a valence band tailing, offering therefore electronic states that may host deeply/shallowly trapped holes. These findings demonstrates that the PL emissions observed for our samples are in agreement with the proposed mechanism about "green and red PL". The different PL behavior in B-AS and B700 therefore remarks that the reduction treatment introduce different defects that have a different PL signatures and influence in different way the photocatalytic activity of brookite samples. These results reflect those of Vequizo et al.[50] who also found that the presence of an appropriate depth of the traps can effectively contribute to enhance the overall photocatalytic activity of TiO_2. They found that in case of as synthesized brookite, the moderate depth of electron traps in comparison with the anatase and the rutile phase with shallow and deep electron traps, respectively, help brookite to be active for the both oxidation and reduction reactions. In our case, instead, we provide evidences that recombinations centers in reduced brookite are those defects that regulate the photo-oxidation reaction during H_2 evolution from methanol/H_2O photoreforming. Further, PL maps recorded in the presence of methanol (Figure 2 in the main text) show for both B-AS and B700 that the radiative recombinations are almost completely quenched in these conditions, confirming the proposed PL mechanism and the fact that during photocatalysis holes are mainly employed for the photo-oxidation reaction.

Figure S41 shows the TRPL of as-synthesized (received) and reduced samples, while Table S11 shows the fitted parameters employed to calculating the average electron life time of each sample. In all cases, the amplitude of the slow component (B_1) is higher than the amplitude of the fast component (B_2). The average electron lifetime (τ_{ave}) of reduced samples, in all cases, is less than that of the corresponding pristine samples. This behavior of reduced TiO_2 samples suggests that after reduction, the defective centers are responsible for a faster charge carrier recombination[51]. Importantly, the results from TPRL measurements demonstrates that the improved photocatalytic activity of our reduced TiO_2 (B700, A500, CB600) is not due to an improved photo-induced charge separation, as shown previously in other TiO_2 systems[52,53]. In contrast, in this case it is regulated by other parameters such as the photo-reactivity of the heterogeneous catalytic sites formed around oxygen vacancies and comprised of several Ti atoms sharing extra charge (see DFT calculations below) and lattice distortions (see XRD analysis).
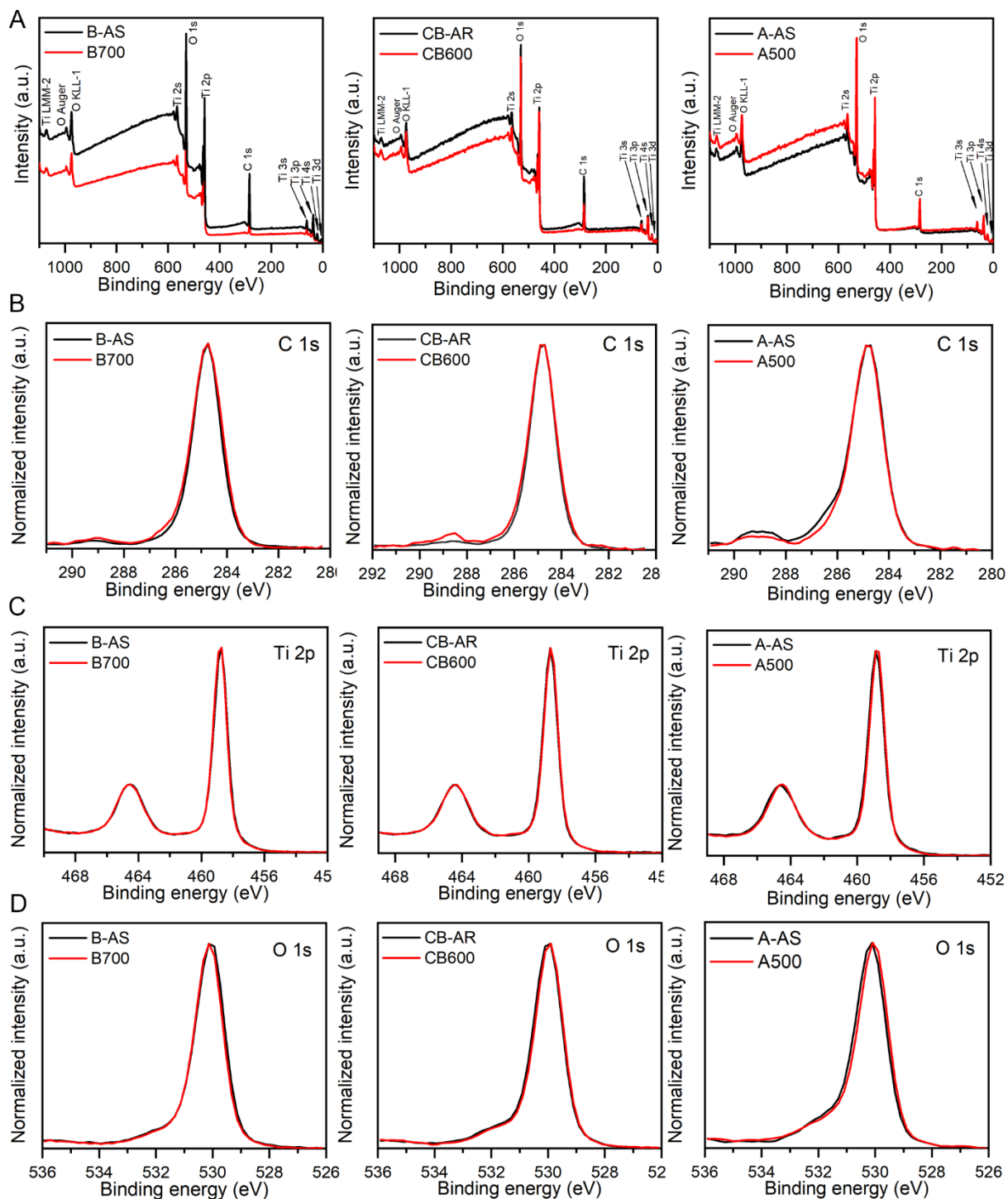
Figure S42. XPS measurements. (A) XPS survey spectra of the pristine and the most photoactive sample of brookite (left), commercial brookite (middle) and anatase(right) (B) High resolution XPS spectra of the pristine and the most photoactive sample of brookite (left), commercial brookite (middle) and anatase.(right) of (B) C *1s*, (C) Ti*2p* and (D) O *1s* regions.
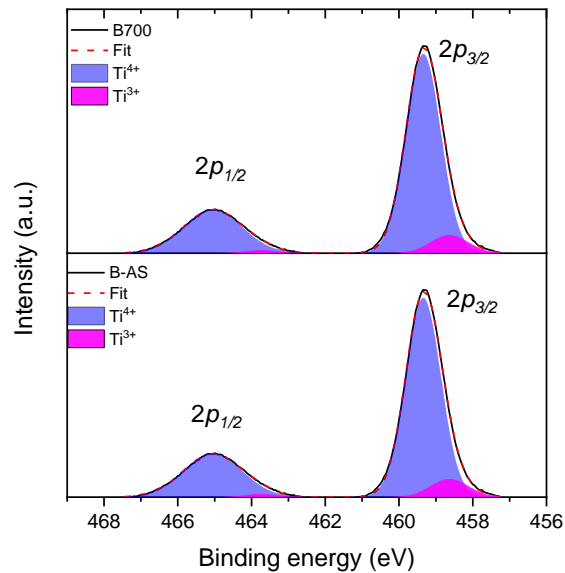
Figure S43. Synchrotron measurements, related to Figure 3. Synchrotron-based XPS spectra in the Ti *2p* region of pristine brookite (B-AS), the most photoactive brookite sample (B700).
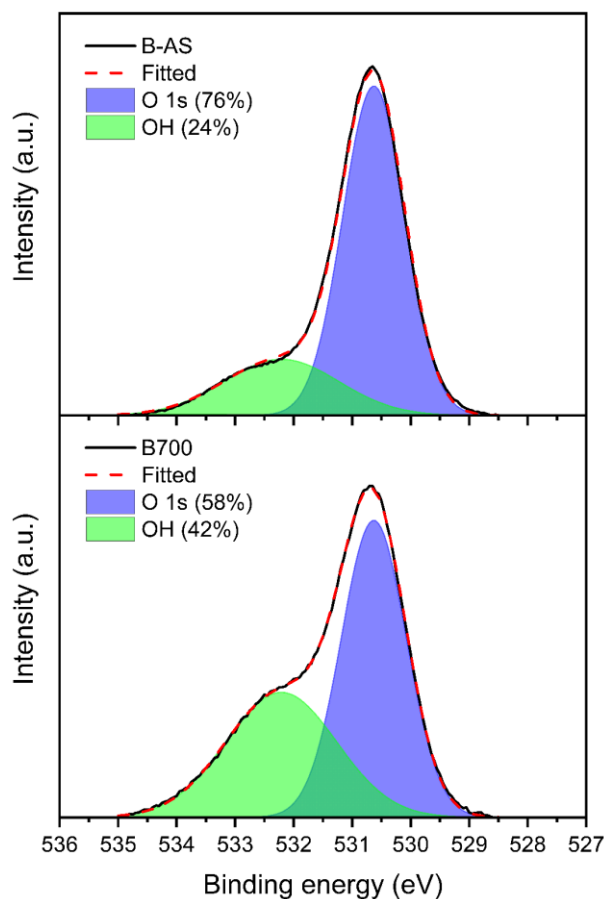

Figure S44. Synchrotron measurements, related to Figure 3. Synchrotron-based XPS spectra of the pristine (top) and the most photoactive sample of brookite (bottom), O *1s* region.
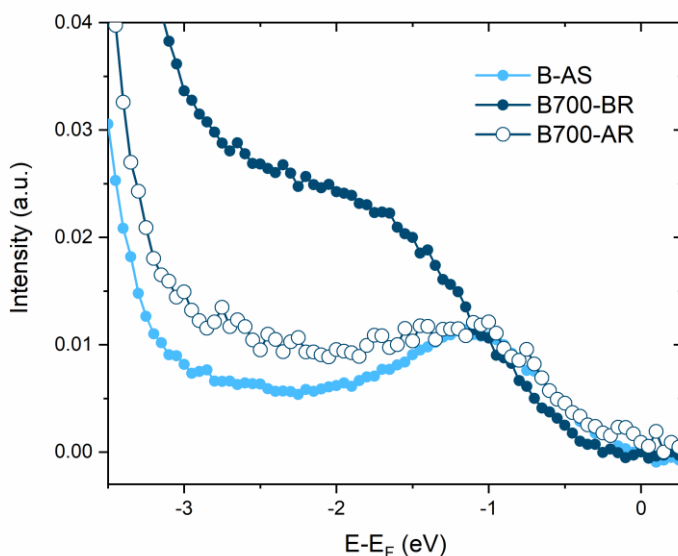
Figure S45. Synchrotron measurements, related to Figure 3. Synchrotron-based photoemission spectra around the valence band (VB) region for the pristine brookite B-AS (light blue, full circles), the reduced brookite before reaction B700-BR (dark blue, full circles), and the reduced brookite after 24 h of photocatalytic reaction B700-AR (dark blue, empty circles).

Note S10. Photoemission spectroscopy, related to Figure 2 and 3, and Figure S42–44. We examined the electronic state of elements at the surface of the as-synthesized (received) and the best reduced samples using an XPS laboratory source. Figure S42 compares the XPS survey spectra of samples before and after reduction treatment. An important finding from these survey spectra is that the samples are not contaminated during the reduction process, as already confirmed by CHN analysis (Table S2), since there is no difference between total XPS survey before and after process. This observation supports our hypothesis that all of the changes in photoactivity of the samples are due to the reduction process and not due to materials contamination. The C $1s$ peak at 284.8 eV was used as a reference for the energy scale to compensate the charging effect of the samples (all spectra were shifted according to this reference). However, the observed difference between XPS spectra of Ti$2p$ and O$1s$ for pristine and reduced samples were not significant. A possible explanation for this might be that the amount of changes in the lattice of TiO$_2$ induced through reduction are below the detection limit of XPS[38] or the reduced species like Ti^{3+} can be easily oxidized by exposure to the ambient air[54]. Since, no difference was detected in XPS analysis between the samples before and after reduction, we used synchrotron-based XPS (VUV-Photoemission beamline, Elettra) to study them in more detail. Figure S43 shows the synchrotron-based XPS Ti$2p$ spectra of the pristine and the most photoactive sample of brookite. There is evidence of an increase in Ti^{3+} species after reduction. Additionally, synchrotron-based XPS study of O$1s$ orbital of the pristine and the most photoactive sample of brookite (Figure S44) reveals about 18% increase in OH groups on the surface of TiO$_2$ after reduction. This supports the water dissociation on superficial defects created upon reduction treatment, see more details in the mechanism part below.
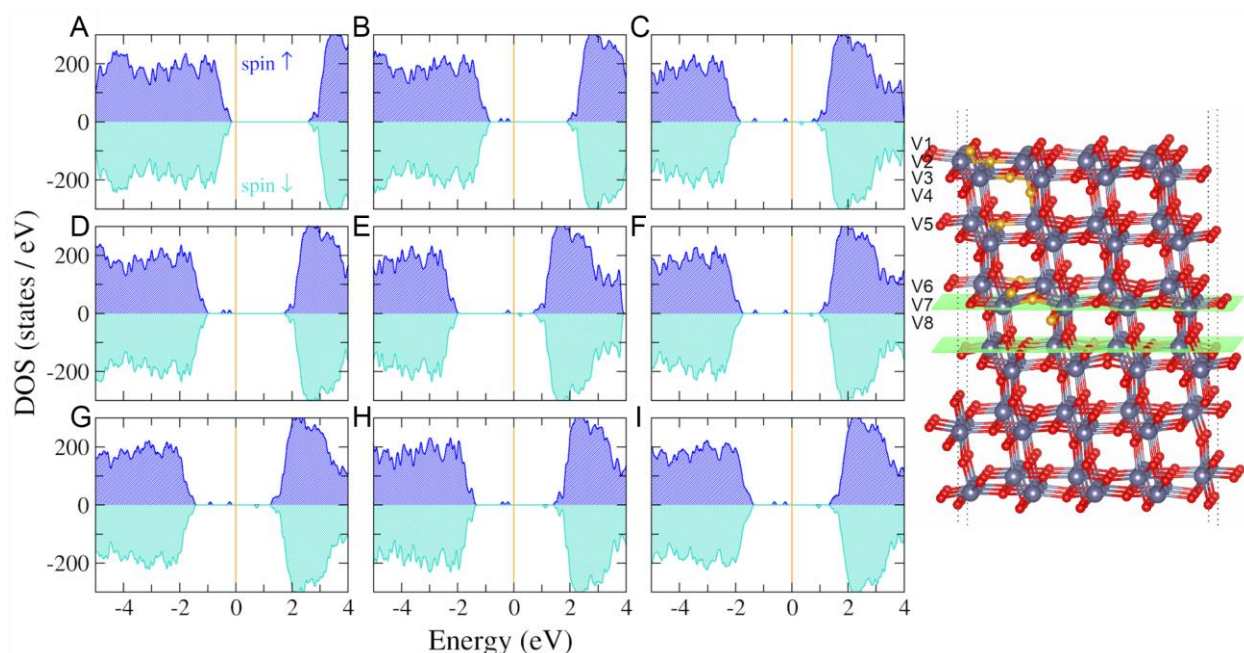
Figure S46. Density functional theory calculations, related to Figure 3. Spin-resolved density of states (DOS) plots of brookite TiO$_2$ supercell exposing the (210) surface. The simulated TiO$_2$ structure is shown on the right side of the panel with Ti atoms plotted in grey, O in red, and O vacancies indicated in orange. The middle part of the slab corresponds to the bulk region of TiO$_2$ enclosed by green planes, and the supercell's boundaries are indicated by the dotted lines. (A) DOS for a perfect slab, (B–I) is for the same slab including one O vacancy denoted by V1–V8 in the structure on the right. All plots are zeroth to the Fermi level. DOS of V2 and V4 were calculated for a fixed geometry to prevent the migration of the vacancy to the on-surface V1 position. The DOS plots clearly show that varying the lattice position (surface, subsurface, bulk) of an oxygen vacancy results in the formation of intragap electronic states with different energy and features.
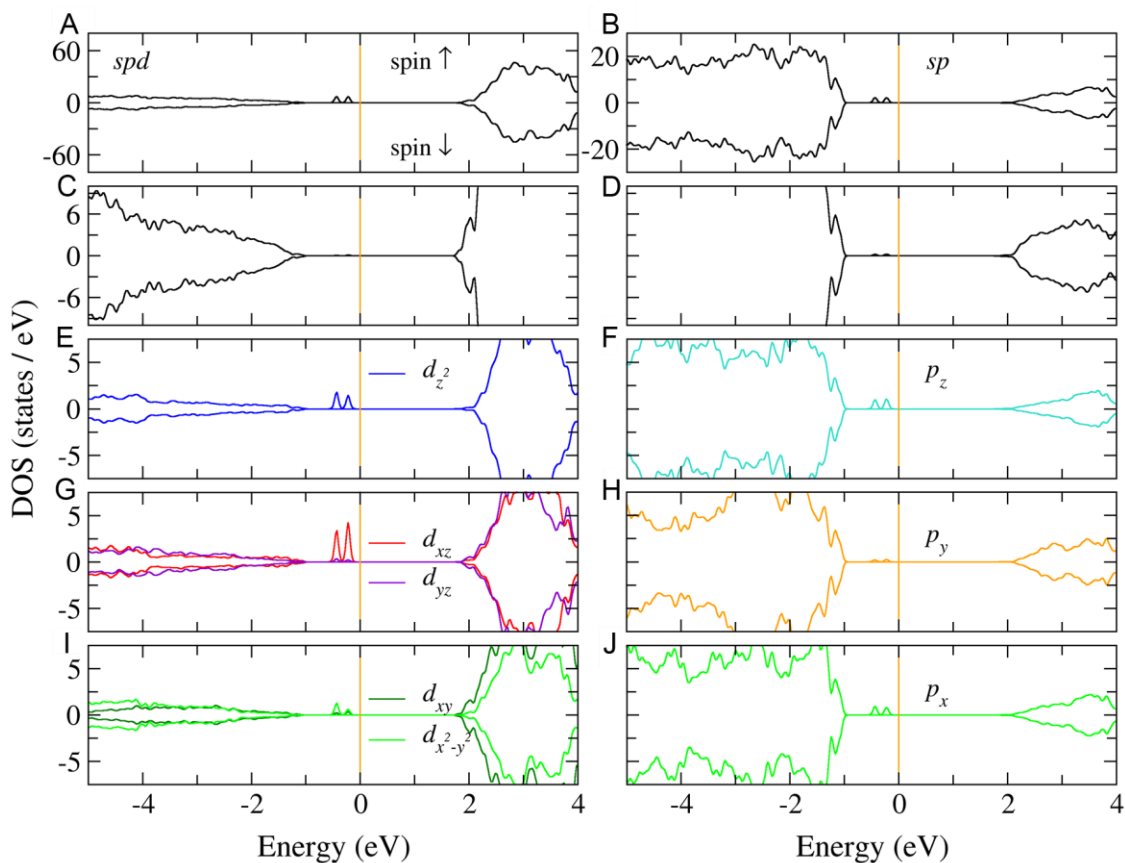
Figure S47. Density functional theory calculations, related to Figure 3. (A) DOS of the surface Ti bilayer and (B) the corresponding O atoms with the missing O atom at V3 position. (C) DOS of subsurface Ti bilayer and (D) the corresponding O atoms. (E–J) Orbital resolved partial DOS for the surface Ti bilayer (E, G, I) and O atoms (F, H, J). All plots are zeroth to EF. It is interesting to note how intragap states are composed by hybridized electronic contributions belonging both to Ti and O atoms.

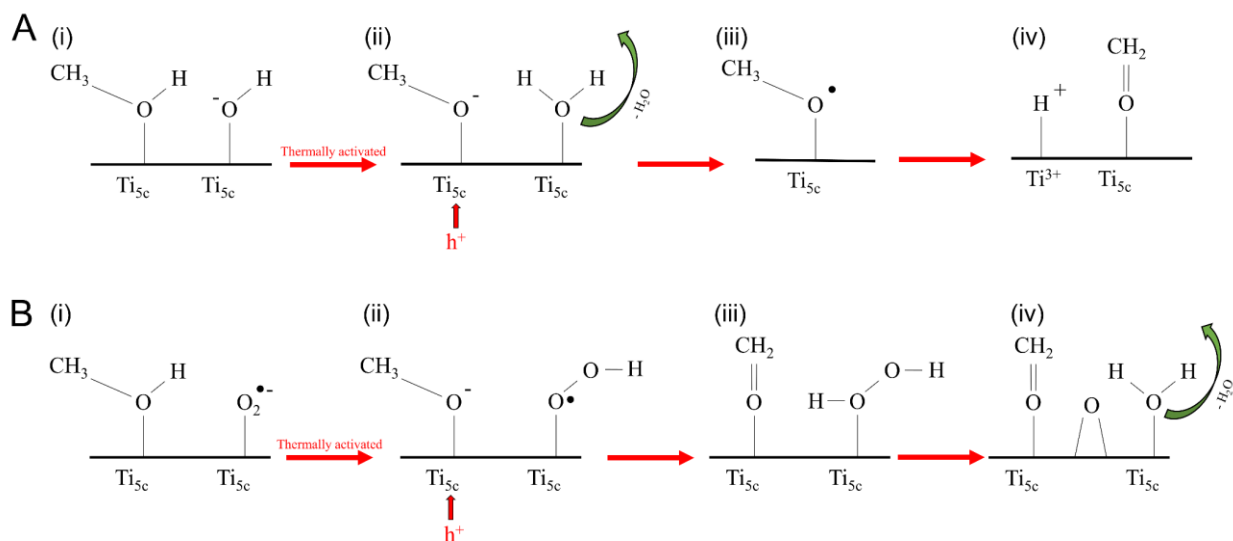**Figure S48. Methanol oxidation mechanism at the brookite TiO$_2$ surface.** (A) Methanol activation by terminal OH$^-$. In step (i) → (ii) the OH reacts with methanol producing H$_2$O and the methoxy group. In (ii) → (iii) the methoxy group accepts a hole from TiO$_2$ substrate (or donates an electron to TiO$_2$) and converts to methoxy radical, while the water molecule is released from the TiO$_2$ surface. In (iii) → (iv) the methoxy radical decomposes to adsorbed formaldehyde and proton ion. (B) Methanol activation by coadsorbed O$_2$. In step (i) → (ii) The superoxide activates the methanol and to methoxy radical and produces the peroxide radical. Then in step (ii) → (iii) such radicals are converted to adsorbed formaldehyde and hydrogen peroxide, respectively. In step (iii) → (iv) the hydrogen peroxide decomposes to water (then released from the TiO$_2$ surface) and a bridging oxygen dimer[55].

Supplemental references

1. Kandiel, T.A., Feldhoff, A., Robben, L., Dillert, R., and Bahnemann, D.W. (2010). Tailored titanium dioxide nanomaterials: Anatase nanoparticles and brookite nanorods as highly active photocatalysts. Chem. Mater. *22*, 2050–2060.
2. Zhao, H., Liu, L., Andino, J.M., and Li, Y. (2013). Bicrystalline TiO_2 with controllable anatase-brookite phase content for enhanced CO_2 photoreduction to fuels. J. Mater. Chem. *1*, 8209–8216.
3. Beltram, A., Romero-Ocaña, I., Josè Delgado Jaen, J., Montini, T., and Fornasiero, P. (2016). Photocatalytic valorization of ethanol and glycerol over TiO_2 polymorphs for sustainable hydrogen production. Appl. Catal. A: Gen *518*, 167–175.
4. Naldoni, A., Montini, T., Malara, F., Mróz, M.M., Beltram, A., Virgili, T., Boldrini, C.L., Marelli, M., Romero-Ocaña, I., Delgado, J.J., et al. (2017). Hot electron collection on brookite nanorods lateral facets for plasmon-enhanced water oxidation. ACS Catal. *7*, 1270–1278.
5. Larson, A.C., and Von Dreele, A.C. (2004). General structure analysis system (GSAS).
6. Weyl, R. (1977). Zeitschrift fuer Kristallographie.
7. http://www.iucr.org/resources/data/datasets/bond-valenceparameters.
8. Williamson, G.K., and Hall, W.H. (1953). X-ray line broadening from filed aluminium and wolfram. Acta metall. *1*, 22–31.
9. Roisnel, T., and Rodríguez-Carvajal, J. (2001). WinPLOTR: A windows tool for powder diffraction pattern analysis. Mater. Sci. Forum *378–381*, 118–123.
10. Rouquerol, F., Rouquerol, J., Llewellyn, P., Maurin, G., Sing, K., (1999). Adsorption by powders and porous solids (Elsevier).
11. Rex, R.E., Knorr, F. J., and McHale, J.L. (2013). Comment on "Characterization of oxygen vacancy associates within hydrogenated TiO_2: A positron annihilation study". J. Phys. Chem *117*, 7949–7951.
12. Stoll, S., and Schweiger, A. (2006). EasySpin, a comprehensive software package for spectral simulation and analysis in EPR. J. Magn. Reson. *178*, 42–55.
13. Kresse, G., and Furthmuller, J. (1996). Efficient iterative schemes for ab initio total-energy calculations using a plane-wave basis set. Phys. Rev. B Condens. Matter Mater. Phys. *54*, 11169–11186.
14. Kresse, G., and Furthmüller, J. (1996). Efficiency of ab-initio total energy calculations for metals and semiconductors using a plane-wave basis set. Comput. Mater. Sci. *6*, 15–50.
15. Blöchl, P.E. (1994). Projector augmented-wave method. Phys. Rev. B Condens. Matter Mater. Phys. *50*, 17953–17979.
16. Kresse, G., and Joubert, D. (1999). From ultrasoft pseudopotentials to the projector augmented-wave method. Phys. Rev. B Condens. Matter Mater. Phys. *59*, 1758–1775.
17. Perdew, J.P., Burke, K., and Ernzerhof, M. (1996). Generalized gradient approximation made simple. Phys. Rev. Lett. *77*, 3865–3868.
18. Perdew, J.P., Burke, K., and Ernzerhof, M. (1997). Generalized gradient approximation made simple (Errata). Phys. Rev. Lett. *78*, 1396–1396.
19. Dudarev, S.L., Botton, G.A., Savrasov, S.Y., Humphreys, C.J., and Sutton, A.P. (1998). Electron-energy-loss spectra and the structural stability of nickel oxide: An LSDA+U study. Phys. Rev. B *57*, 1505–1509.
20. Morgan, B.J., and Watson, G.W. (2009). Polaronic trapping of electrons and holes by native defects in anatase TiO_2. Phys. Rev. B *80*, 2331021–2331024.
21. Holmström, E., Ghan, S., Asakawa, H., Fujita, Y., Fukuma, T., Kamimura, S., Ohno, T., and Foster, A.S. (2017). Hydration structure of brookite TiO_2 (210). J. Phys. Chem *121*, 20790–20801.
22. Naldoni, A., Allieta, M., Santangelo, S., Marelli, M., Fabbri, F., Cappelli, S., Bianchi, C.L., Psaro, R., and Dal Santo, V. (2012). Effect of nature and location of defects on bandgap narrowing in black TiO_2 nanoparticles. J. Am. Chem. Soc. *134*, 7600–7603.
23. Naldoni, A., Altomare, M., Zoppellaro, G., and Liu, N. (2019). Photocatalysis with reduced TiO_2 : from black TiO_2 to cocatalyst- free hydrogen production. ACS Catal. *9*, 345–364.
24. Bersani, D., Lottici, P.P., and Ding, X. (1998). Phonon confinement effects in the Raman scattering by TiO_2 nanocrystals. Appl. Phys. Lett. *72*, 73–75.
25. Parker, J.C., and Siegel, R.W. (1990). Calibration of the Raman spectrum to the oxygen stoichiometry of nanophase TiO_2. Appl. Phys. Lett. *57*.
26. Fauchet, I.H.C. and P.M. (1986). The effects of microcrystal size and shape of the one phonon raman spectra of crystalline semiconductor. Solid State Commun. *58*, 739–741.

27. Venkatasubbu, G.D., Ramakrishnan, V., Sasirekha, V., Ramasamy, S., and Kumar, J. (2014). Influence of particle size on the phonon confinement of TiO_2 nanoparticles. J. Exp. Nanosci. *9*, 661–668.
28. Fisica, D., Infm, C., Chimica, S., Parma, U., and Scienze, V. (1993). Raman scattering characterization of gel-derived titania glass. J. Mater. Sci. *28*, 177–183.
29. Tauc, J., Grigorovici, R., Vancu, A. (1966). Optical properties and electronic structure of amorphous germanium. Phys. Stat. Sol. *627*, 627–637.
30. Escobedo-Morales, A., Ruiz-López, I.I., Ruiz-Peralta, M.deL., Tepech-Carrillo, L., Sánchez-Cantú, M., and Moreno-Orea, J.E. (2019). Automated method for the determination of the band gap energy of pure and mixed powder samples using diffuse reflectance spectroscopy. Heliyon *5*, 1–19.
31. Mohajernia, S., Andryskova, P., Zoppellaro, G., Hejazi, S., Kment, S., Zboril, R., Schmidt, J., and Schmuki, P. (2020). Influence of Ti^{3+} defect-type on heterogeneous photocatalytic H_2 evolution activity of TiO_2. J. Mater. Chem. A *8*, 1432–1442.
32. Makuła, P., Pacia, M., and Macyk, W. (2018). How to correctly determine the band gap energy of modified semiconductor photocatalysts based on UV-Vis spectra. J. Phys. Chem. Lett. *9*, 6814–6817.
33. Urbach, T. (1953). The long-wavelength edge of photographic sensitivity and of the electronic absorption of solids. Phys. Rev. *92*, 1324.
34. Rai, R.C. (2013). Analysis of the Urbach tails in absorption spectra of undoped ZnO thin films. J. Appl. Phys. *113*, 153508.
35. John, S., Soukoulis, C., Cohen, M.H., and Economou, E.N. (1986). Theory of electron band tails and the Urbach optical-absorption edge. Phys. Rev. Lett. *57*, 1777–1780.
36. Akshay, V.R., Arun, B., Mandal, G., and Vasundhara, M. (2019). Visible range optical absorption, Urbach energy estimation and paramagnetic response in Cr-doped TiO_2 nanocrystals derived by a sol–gel method. Phys. Chem. Chem. Phys. *21*, 12991–13004.
37. H. Tang, F. Levy, H. Berger, P.E.S. (1995). Urbach tail of anatase TiO_2. Phys. Rev. B *52*, 7771–7774.
38. Mohajernia, S., Andryskova, P., Zoppellaro, G., Hejazi, S., Kment, S., Zboril, R., Schmidt, J., and Schmuki, P. (2020). Influence of Ti^{3+} defect-type on heterogeneous photocatalytic H_2 evolution activity of TiO_2. Journal of Materials Chemistry A *8*, 1432–1442.
39. Mascaretti, L., Russo, V., Zoppellaro, G., Lucotti, A., Casari, C.S., Kment, Š., Naldoni, A., and Li Bassi, A. (2019). Excitation wavelength- and medium-dependent photoluminescence of reduced nanostructured TiO_2 films. J. Phys. Chem. C *123*, 11292–11303.
40. Liqiang, J., Yichun, Q., Baiqi, W., Shudan, L., Baojiang, J., Libin, Y., Wei, F., Honggang, F., and Jiazhong, S. (2006). Review of photoluminescence performance of nano-sized semiconductor materials and its relationships with photocatalytic activity. Sol. Energy Mater Sol. Cells *90*, 1773–1787.
41. Gerosa, M., Bottani, C.E., Caramella, L., Onida, G., Di Valentin, C., and Pacchioni, G. (2015). Defect calculations in semiconductors through a dielectric-dependent hybrid DFT functional: The case of oxygen vacancies in metal oxides. J. Chem. Phys. *143*.
42. Shi, J., Chen, J., Feng, Z., Chen, T., Lian, Y., Wang, X., and Li, C. (2007). Photoluminescence characteristics of TiO_2 and their relationship to the photoassisted reaction of water/methanol mixture. J. Phys. Chem. C *111*, 693–699.
43. Mercado, C.C., Knorr, F.J., McHale, J.L., Usmani, S.M., Ichimura, A.S., and Saraf, L. V. (2012). Location of hole and electron traps on nanocrystalline anatase TiO_2. J. Phys. Chem. C *116*, 10796–10804.
44. Vequizo, J.J.M., Kamimura, S., Ohno, T., and Yamakata, A. (2018). Oxygen induced enhancement of NIR emission in brookite TiO_2 powders: Comparison with rutile and anatase TiO_2 powders. Phys. Chem. Chem. Phys. *20*, 3241–3248.
45. Pallotti, D.K., Passoni, L., Maddalena, P., Di Fonzo, F., and Lettieri, S. (2017). Photoluminescence mechanisms in anatase and rutile TiO_2. J. Phys. Chem. C *121*, 9011–9021.
46. Mercado, C., Seeley, Z., Bandyopadhyay, A., Bose, S., and McHale, J.L. (2011). Photoluminescence of dense nanocrystalline titanium dioxide thin films: Effect of doping and thickness and relation to gas sensing. ACS Appl. Mater. Interfaces *3*, 2281–2288.
47. Knorr, F.J., and McHale, J.L. (2013). Spectroelectrochemical photoluminescence of trap states of nanocrystalline TiO_2 in aqueous media. J. Phys. Chem. C *117*, 13654–13662.
48. Knorr, F.J., Mercado, C.C., and McHale, J.L. (2008). Trap-state distributions and carrier transport in pure and mixed-phase TiO_2: Influence of contacting solvent and interphasial electron transfer. J. Phys. Chem. C *112*, 12786–12794.

49. Mercado, C.C., McHale, J.L. Defect photoluminescence of TiO_2 nanotubes. (2010). MRS Online Proceedings Library *1268*, 310.

50. Vequizo, J.J.M., Matsunaga, H., Ishiku, T., Kamimura, S., Ohno, T., and Yamakata, A. (2017). Trapping-induced enhancement of photocatalytic activity on brookite TiO_2 powders: Comparison with anatase and rutile TiO_2 powders. ACS Catal. *7*, 2644–2651.

51. Yan, Y., Han, M., Konkin, A., Koppe, T., Wang, D., Andreu, T., Chen, G., Vetter, U., Morante, J.R., and Schaaf, P. (2014). Slightly hydrogenated TiO_2 with enhanced photocatalytic performance. J. Mater. Chem. A *2*, 12708–12716.

52. Wu, Z., Cao, S., Zhang, C., and Piao, L. (2017). Effects of bulk and surface defects on the photocatalytic performance of size-controlled TiO_2 nanoparticles. Nanotechnology *28*.

53. Alsalka, Y., Hakki, A., Schneider, J., and Bahnemann, D.W. (2018). Co-catalyst-free photocatalytic hydrogen evolution on TiO_2: Synthesis of optimized photocatalyst through statistical material science. Appl. Catal. B *238*, 422–433.

54. Mohajernia, S., Hejazi, S., Mazare, A., Nguyen, N.T., and Schmuki, P. (2017). Photoelectrochemical H_2 generation from suboxide TiO_2 nanotubes: visible-light absorption versus conductivity. Chem. Eur. J. *23*, 12406–12411.

55. Setviń, M., Aschauer, U., Scheiber, P., Li, Y.F., Hou, W., Schmid, M., Selloni, A., and Diebold, U. (2013). Reaction of O_2 with subsurface oxygen vacancies on TiO_2 anatase (101). Science *341*, 988–991.